An improved representation of aerosol in the ECMWF IFS-COMPO 49R1 through the integration of EQSAM4Climv12 - a first attempt at simulating aerosol acidity

Samuel Rémy[1], Swen Metzger[2], Vincent Huijnen[3], Jason E Williams[3], and Johannes Flemming[4]

[1]HYGEOS, Lille, France
[2]Eco-Serve, ResearchConcepts Io GmbH, Freiburg, Germany
[3]R and D Weather and Climate modeling, Royal Netherlands Meteorological Institute, De Bilt, Netherlands
[4]European Centre for Medium Range Weather Forecasts, Reading, UK and Bonn, Germany

Correspondence: Samuel Rémy (sr@hygeos.com)

Abstract. The atmospheric composition forecasting system used to produce the CAMS forecasts of global aerosol and trace gases distributions, IFS-COMPO, undergoes periodic upgrades. In this study we describe the development of the future operational cycle 49R1, and focus on the implementation of the thermodynamical model EQSAM4Clim version 12 to represent gas-aerosol partitioning processes for the nitric acid/nitrate and a ammonia/ammonium couples and to compute diagnostic aerosol, cloud and precipitation pH values at the global scale. This information on aerosol acidity influences the simulated tropospheric chemistry processes associated with aqueous phase chemistry and wet deposition. The other updates of cycle 49R1 concern wet deposition, changes in the sea-salt aerosol emissions and in the dust optics, as well as the assumed size distribution used for the calculation of sulfate aerosol optics. The implementation of EQSAM4Clim significantly improves the partitioning of reactive nitrogen compounds, decreasing surface concentrations of both nitrate and ammonium in particulate phase, which reduces PM2.5 biases for Europe, U.S. and China, especially during summertime. For aerosol optical depth there is generally a decrease in the simulated biases for wintertime, and for some regions an increase in the bias for summertime. Improvements in the simulated Ångström exponent is noted for almost all regions, resulting in generally a good agreement with observations. The diagnostic aerosol and precipitation pH calculated by EQSAM4Clim have been compared against results from ground observations and previous simulations. For precipitation pH, the annual mean values show a relatively goof agreement with the regional observational datasets, while for aerosol pH the simulated values over continents are quite close to those simulated by ISORROPIA-II. The use of aerosol acidity only has a relatively smaller impact on the aqueous-phase production of sulphate as compared to the changes in gas-to-particle partitioning induced by the use of EQSAM4Clim.

1   Introduction

The Copernicus Atmosphere Monitoring Service (CAMS) provides daily global analysis and 5-days forecasts of atmospheric composition (aerosols, trace gases and greenhouse gases) (Peuch et al. (2022)). CAMS is coordinated by the European Centre for Medium Range Weather Forecasts (ECMWF) and uses, for its global component, the Integrated Forecasting System (IFS), with extensions to represent aerosols, trace and greenhouses gases, being called "IFS-COMPO" (also pre-

viously known as "C-IFS", Flemming et al. (2015)). In this article, we focus on the version of IFS-COMPO that simulates aerosols and trace gases. IFS-COMPO is composed of IFS(AER) for aerosols, as described in Rémy et al. (2022) while the atmospheric chemistry is based on the chemistry module as described in Williams et al. (2022) for the troposphere and Huijnen et al. (2016) for the stratosphere. Different versions of IFS-COMPO have also been used to produce the MACC Reanalysis (Inness et al., 2013), the CAMS interim reanalysis (Flemming et al., 2017) and the CAMS reanalysis (Inness et al., 2019). Here, we primarily focus on tropospheric processes and use a version of IFS-COMPO without the application of stratospheric chemistry. This model configuration is also referred to as IFS(CB05). Please note however that in the operational context IFS-COMPO including stratospheric chemistry is used since the operational implementation of cycle 48R1 on 27th of June 2023 (hereafter referred to as CY48R1). All of the components of CY48R1 IFS-COMPO are described in detail in the publicly available IFS documentation (ECMWF, 2023), available at https://www.ecmwf.int/en/elibrary/81374-ifs-documentation-cy48r1-part-viii-atmospheric-composition. Besides its use in CAMS, a different version of IFS(AER) has been adopted within the Météo-France CNRM climate model system (Michou et al., 2015); an older version of IFS-COMPO, based on cycle 43R3, is also provided as part of an OpenIFS release (Huijnen et al., 2022), while the release of OpenIFS based on cycle 48R1 is in preparation and planned for December 2023.

IFS-COMPO has been continually updated over time, with yearly or twice yearly upgrades of the operational forecasting system that followed and included upgrades of the operational IFS. The code revisions that are integrated into the operational version of IFS-COMPO must satisfy the two conditions (one qualitative, one quantitative) that they bring the model closer to "physical" reality, i.e. that more processes and/or species are represented, and that they improve the skill scores of the main products against observations. This article describes an upgrade of IFS-COMPO that will be implemented in cycle 49R1 (hereafter referred to as CY49R1), aimed at a better representation of aerosol composition and gas/particle partitioning processes, through the implementation of the thermodynamical model EQSAM4Clim (Metzger et al., 2016) to allow the representation of aerosol, cloud and precipitation acidity in the IFS-COMPO chemical forecasting system. The other aerosol modeling updates of CY49R1 are also briefly introduced. CY49R1 is planned to become operational in the autumn 2024.

In this article we focus on the update of the representation of aerosol, cloud and precipitation acidity in the IFS-COMPO chemical forecasting system. With increasing complexity of the representation of atmospheric aerosols in air pollution, weather and climate models, derived properties, such as the aerosol acidity, receive more and more attention. The solution's acidity is impacted by the aerosol composition and the water content, which itself depends on aerosol composition and meteorology. A recent literature review of Pye et al. (2020) summarizes the current state of knowledge on the acidity of atmospheric condensed phases, specifically particles and cloud droplets, while Tilgner et al. (2021) and Ault (2020) reviews the current state of knowledge with a focus on the acidity of aerosol and cloud systems, which involves both inorganic and organic aqueous phase chemistry. In addition, Shah et al. (2020) addresses the global modeling of aerosol, cloud and precipitation acidity, and acid inputs to ecosystems using the GEOS-Chem Chemistry Transport Model (CTM). Nault et al. (2021) highlights the challenges of simulating aerosol acidity, showing that models often underestimate aerosol acidity in remote regions. Finally, Karydis et al. (2021) address how alkaline compounds control atmospheric aerosol acidity in the EMAC model, where alkaline compounds, notably ammonium (NH_4^+), and to a lesser extent crustal cations e.g. Ca^{2+}, which buffer aerosol pH at global

scale. In the review of Tilgner et al. (2021) it is concluded that although many advances have been made in our understanding of acidity-driven and acid-catalyzed chemical processes, many open issues still need to be addressed for a better understanding of impact on key pollutants. More recently, a more complex representation of aerosol acidity and its impact on multiphase chemistry has been introduced in the EC-EARTH Earth System Model, as described in Myriokefalitakis et al. (2022).

Ammonium nitrate (NH_4NO_3) is a key component of anthropogenic aerosols and represents a growing share of particulate matter with aerodynamical diameter below 2.5 micron (PM2.5), especially in light of the decreasing trend in sulphur dioxide (SO_2) emissions (Bellouin et al., 2011). In IFS-COMPO, NH_4NO_3 is formed through gas-particle partitioning processes, parameterized from Hauglustaine et al. (2014), while other NO_3^- compounds are formed from heterogeneous reactions on desert dust and sea-salt particles (see Rémy et al. (2019) and ECMWF (2023) for more details). The implementation of the thermodynamical model EQSAM4Clim aims to bring a more realistic representation of the production of NH_4^+ and NO_3^- through both gas-to-particle processes and heterogeneous reactions, which in turn should improve the simulated PM2.5 and AOD, two key CAMS forecast products. EQSAM4Clim also provides an estimate of the aerosol water and aerosol acidity, which allows the diagnosis of the acidity in aerosols, clouds and precipitation. This information can then be used in the relevant multiphase chemistry processes - namely aqueous phase chemistry and wet deposition (via the solubility computation). A better representation of gas-particle partitioning is also expected to bring an improvement in the simulated sulphur (S) and nitrogen (N) deposition terms, which are set to become new products of the CAMS portfolio because of their impact on pristine environments. Increased N deposition can cause an exceedance of critical loads in terms of the cumulative annual deposition on ecosystems (Sun et al., 2020). Elevated S and N deposition are also associated with a host of environmental issues such as acidification and eutrophication of the terrestrial system, while increasing nitrogen deposition could enhance the carbon uptake by land processes (Reay et al., 2008), similarly to phosphorus deposition (Wang et al., 2017).

Briefly, the contents of this article are as follows. In section 2 we describe the integration of EQSAM4Clim version 12 into IFS-COMPO, and how it has been coupled to other components of the system and the new pH diagnostics that have been implemented. Other atmospheric composition model updates of CY49R1 are also presented. In section 3 we compare IFS-COMPO simulations for 2019 using cycles 48R1 and pre-49R1 (i.e. including atmospheric composition model updates planned for CY49R1, on top of CY48R1) in terms of budgets and model fields. In section 4, the simulated AOD and PM2.5 are evaluated. We also focus on the impact of EQSAM4Clim on the oxidized and reduced N chemistry cycles, and on the subsequent impact on simulated surface concentration of oxidized and reduced nitrogen species, as well as PM2.5 and AOD. The new aerosol and precipitation pH diagnostics from IFS-COMPO are also compared against selected validation datasets: aerosol pH from ISORROPIA-II (Fountoukis and Nenes (2007)) simulations using ground observations from Zhang et al. (2021), simulated aerosol pH from Rosanka et al. (2024) and precipitation pH from routine monitoring networks over Europe, Asia and U.S.

2 Implementation of EQSAM4Clim in IFS-COMPO and other updates of CY49R1

2.1 General introduction to IFS-COMPO and IFS(AER) before CY49R1

The default tropospheric chemistry scheme in IFS-COMPO, also referred to as "IFS(CB05)", is a reduced version of that developed by Yarwood et al. (2005) as described in Williams et al. (2013) and Huijnen et al. (2019), and further updated in Williams et al. (2022) to expand on NOy species and isoprene chemistry. Photolysis is calculated online using the modified band approach as developed in Williams et al. (2012) and embedded in IFS-COMPO, where aerosol effects are included in the calculation of photolysis rates. In this section, a description of the general features of cycle 48R1 IFS-COMPO is proposed. For further details, we refer the reader to the official documentation of cycle 48R1 IFS-COMPO, available at https://www.ecmwf.int/en/elibrary/81374-ifs-documentation-cy48r1-part-viii-atmospheric-composition.

The aerosol component of IFS-COMPO is a bulk aerosol scheme for all species except sea salt aerosol and desert dust, for which a sectional approach is preferred, with three bins for each of these two species. As such, it is often denoted as a "bulk–bin" scheme; IFS(AER) derives from the Laboratoire d'Optique Atmosphérique/Laboratoire de Météorologie Dynamique - Zoom (LOA/LMDZ) model (Boucher et al. (2002), Reddy et al. (2005)) and uses a mass mixing ratio as the prognostic variable of the aerosol tracers. Since the implementation of operational cycle 48R1 in June 2023, the prognostic species are sea salt, desert dust, organic matter (OM), black carbon (BC), sulfate, NO_3^-, NH_4^+ and secondary organics (SOA). IFS(AER) is by default coupled with the tropospheric chemistry of IFS-COMPO.

Desert dust is represented with three size bins, with radius bin limits at 0.03, 0.55, 0.9 and 20 μm. Sea salt aerosol is also represented with three size bins, with radius bin limits of 0.03, 0.5, 5 and 20 μm at 80 % relative humidity. All of the sea salt aerosol parameters (concentration, emission, deposition) are expressed at 80 % relative humidity; this is in contrast to the other aerosol species in IFS(AER), which are expressed as dry mixing ratio. The sea salt aerosol mass mixing ratio, as well as the emissions, burden and sink diagnostics, need to be divided by a factor of 4.3 to convert to dry mass mixing ratio in order to account for the hygroscopic growth and change in particle density. There is no mass transfer between bins for either dust or sea salt.

The OM and BC aerosol species consists of their hydrophilic and hydrophobic fractions, with the ageing processes transferring mass from the hydrophobic to hydrophilic components. Sulfate aerosols is represented by one prognostic variable. The NO_3^- species consists of two prognostic variables that represent fine NO_3^- produced by gas–particle partitioning and coarse NO_3^- produced by heterogeneous reactions of nitric acid on dust and sea salt particles. Finally, the secondary organics species consists of two tracers, that represent biogenic and anthropogenic Secondary Organic Aerosol (SOA). In all, the aerosol component of IFS-COMPO is thus composed of 16 variables in its operational configuration, which allows for a relatively limited consumption of computing resources.

One of the most important features of the recent upgrades of IFS-COMPO is the increasing integration of aerosol and chemistry. The sulphur and nitrogen cycles are represented across the aerosol module (for particulate species) and the chemistry module (for gaseous species, and the production rate of particulate sulfate). The aerosol module provides supplementary input to the chemistry in order to better represent heterogeneous reactions and the impact of aerosols on photolysis rates.

The production scheme of NO_3^- and NH_4^+ through gas/particle partitioning processes, and of NO_3^- from heterogeneous reactions on dust and sea salt particles, is described in Rémy et al. (2019) and has been adapted from Hauglustaine et al. (2014). The gas/particle partitioning part uses the first version of the EQuilibrium Simplified Aerosol Model (EQSAM, Metzger et al. (2002)). These parameterisations use meteorological parameters as input which is provided by IFS as well as the gaseous precursors: nitric acid (HNO_3) and ammonia (NH_3) which are provided by the chemistry module. The gas-particle partitioning scheme estimates NO_3^- and NH_4^+ production through the neutralization of HNO_3 by the NH_3 remaining after neutralisation by sulphuric acid. The formation of NO_3^- from heterogeneous reactions of HNO_3 with calcite (a component of dust aerosol) and sea salt particles is accounted for.

IFS-COMPO is run operationally at a horizontal resolution of T_L511 (40 km grid cell), 137 levels over the vertical and a time step of 900s. A definition of the vertical levels can be found at <https://confluence.ecmwf.int/display/UDOC/L137+ model+level+definitions>. Prognostic aerosols are used as an input of the IFS radiation scheme to compute the direct radiative effect of aerosols. IFS uses a semi-implicit semi Lagrangian (SL) advection scheme (Hortal, 2002). It is computationally efficient but does not conserve the tracer mass when the flow is convergent or divergent, which is often the case in the presence of orographic features. To compensate for this, mass fixers are used for greenhouse gases (Agusti-Panareda et al., 2017), for trace gases (Diamantakis and Flemming, 2014) and for aerosols.

2.2 Description of EQSAM4Clim version 12 and integration into IFS-COMPO for CY49R1

For the integration of EQSAM4Clim into IFS-COMPO we use version 12 (v12), which includes a revised calculation of aerosol acidity. This version of EQSAM4Clim is described in detail in Metzger et al. (2023); its main features are summarized below. The overall gas/liquid/solid partitioning and parameterization for calculating aerosol water uptake is identical to that described in Metzger et al. (2016). In contrast to the original version of EQSAM (Metzger et al., 2002), EQSAM4Clim is based on a compound specific single-solute coefficient (ν_i), which was introduced in Metzger et al. (2012) to accurately parameterise the single solution hygroscopic growth, considering the Kelvin effect. This ν_i-approach accounts for the water uptake of concentrated nanometer-sized particles up to dilute solutions, i.e. from the compounds relative humidity of deliquescence (RHD) up to supersaturation, using the Köhler theory (Köhler, 1936). EQSAM4Clim extends the ν_i-approach to multicomponent mixtures, including semi-volatile NH_4^+ compounds and major crustal elements such as Ca^{++}, Na^+ and Mg^{2+}. A strength of EQSAM4Clim is that the entire gas–liquid–solid aerosol phase partitioning and water uptake, including major mineral cations, can be solved analytically without iterations and numerical noise, making EQSAM4Clim suited for climate and high resolution NWP applications.

EQSAM4Clim calculates the equilibrium aerosol composition and aerosol associated water mass (AW) through the neutralization of anions by cations, which yields numerous salt compounds. All salt compounds (except calcium sulphate, $CaSO_4$) partition between the liquid and solid aerosol phase, depending on atmospheric temperature (T), relative humidity (RH), AW and the T-dependent RHD of (i) single solute compound solutions, or (ii) of mixed salt solutions (Metzger et al., 2012). EQSAM4Clim outputs the aerosol pH along with the concentration of aerosol species (lumped cations, anions), as well as the AW. An application of EQSAM4Clim to AW and optical depth (AOD) calculations has been presented in Metzger et al. (2018).

5
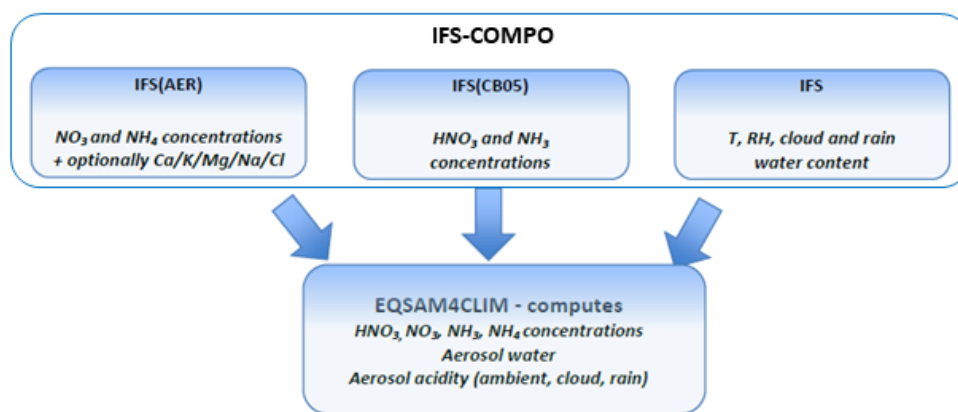
Figure 1. Schematic showing the inputs and outputs of EQSAM4Clim as implemented into IFS-COMPO.

A schematic of the integration of EQSAM4Clim into IFS-COMPO is shown in Figure 1. EQSAM4Clim takes as input, for each model time-step and within a given grid box, particle number and size, (i) T and RH as provided by the meteorological component of IFS-COMPO, (ii) the aerosol precursor gases, i.e., major oxidation products of natural and anthropogenic air pollution represented by NH_3 and HNO_3 from tropospheric chemistry, and (iii) the ionic aerosol concentrations lumped (liquid+solid) anions: sulphate (SO_4^{2-}), nitrate (NO_3^-), chloride (Cl^-), and lumped (liquid+solid) cations: ammonium (NH_4^+), sodium (Na^+), potassium (K^+), magnesium (Mg^{2+}), and calcium (Ca^{2+}) as provided by IFS(AER).

It should be noted that input values for the application of EQSAM4Clim, i.e., HNO_3/NO_3^-, NH_3/NH_4^+ and SO_4^{2-} are prognostic species and directly provided by IFS-COMPO, while the mineral anions (Cl^-) and cations (Na^+, K^+, Mg^{2+} and Ca^{2+}), must be derived from the existing tracers. HCl is not yet coupled as the CB05 scheme currently does not contain tropospheric halogen chemistry. For Ca^{2+}, the approach chosen is the same as that described in Rémy et al. (2019): an experimental version of IFS-COMPO that decomposes dust into a simplified mineralogical composition has been developed and is used to compute a climatology of airborne calcite. This experimental IFS-COMPO version uses as an input the dataset of soil mineralogical composition of Journet et al. (2014) to provides an estimate of the calcite content of airborne dust. Geographically dependent scaling factors derived from this climatology are used to estimate the calcium content of dust, which varies between 5-10% for fine/coarse dust and 2-5% for super-coarse dust. For Cl^- and Na^+ input is derived from sea-salt aerosol assuming the mean mass fractions of 55.0% Cl^- and 30.6% Na^+ from dry sea-salt aerosol mass, following Myriokefalitakis et al. (2022). Assuming a 80% relative humidity over the ocean, this translates into 12.8% and 7.1% of the mass of sea-salt aerosol at 80% RH. The contribution of Na^+, K^+ Mg^{2+} from desert dust is derived from the desert dust tracers using constant scaling factors of 1.2%, 1.5%, and 0.9%, following the approach in EC-Earth (Myriokefalitakis et al., 2022).

2.2.1 Computation of pH diagnostics

EQSAM4Clim calculates the pH of the solution, as governed by the H^+, from the electro-neutrality in solution after neutralization of all available anions by all available cations, by additionally accounting for the auto-dissociation of water, but without the dissolution and dissociation of aerosol precursor gases (e.g. SO_2) and weak acids (e.g. HCOOH) as this is considered in the default aqueous phase chemistry module of IFS-COMPO. Based on the RHD of the single solutes in the (mixed) solution liquid/solid partitioning is calculated, whereby all compounds for which the RH is below the RHD are assumed to be precipitated, such that a solid and liquid phase can co-exist. The liquid-solid partitioning is strongly influenced by mineral cations and, in turn, largely determines the aerosol pH, which is also impacted by the estimated amount of AW. Because some IFS-COMPO aerosol species, such as black carbon, organic matter and secondary organics are not used in EQSAM4Clim, an amount of diagnostic aerosol water computed using relative humidity dependent growth factors for these aerosol species is used as an input to EQSAM4Clim to contribute to the estimation of aerosol acidity. This diagnostic aerosol water input of EQSAM4Clim also include water from the coarse and super coarse sea-salt aerosol. More detail on how aerosol/cloud/precipitation pH is computed can be found in Metzger et al. (2023). Please note that the chemical domain-dependent correction factor described in Metzger et al. (2023) is not used in the implementation of EQSAM4Clim v12 in the IFS, although it is planned to include it in later IFS-COMPO upgrades.

The cloud and precipitation pH for each grid box are computed as the cumulative contribution of aerosol acidity, as computed by EQSAM4Clim, and of dissolved CO_2, methane sulphonic acid (MSA), HSO_3^- and SO_2. In CY49R1, the $[H]^+$ contribution from formic acid (HCOOH) and acetic acid (CH_3COOH) is also included.

2.2.2 Coupling with aqueous phase chemistry

The pH of cloud droplets affects the uptake of trace gases in cloud droplets, and hence aqueous phase chemistry in IFS(CB05). With regard to aqueous phase chemistry, the diagnostic of cloud pH is used to compute the fraction of gaseous SO_2 dissolved in the aqueous phase, which can subsequently be oxidised to SO_4^{2-}. More precisely, the cloud pH diagnostic is used to determine the fraction of dissolved SO_2 which exists as $SO_2.H_2O$, bisulphite (HSO_3^-) and bisulphate (SO_3^{2-}) using pKa dissociation equilibrium values of 1.2 and 7.2, respectively. The oxidation to SO_4^{2-} is then calculated as the sum of the fraction of S(IV) in the form HSO_3^-/SO_3^{2-} reacting with O_3 and H_2O_2, the two principal routes for aqueous phase SO_4^{2-} production using established reaction rate data (Seinfeld and Pandis, 2006). The transition metal catalysed routes for S(IV) oxidation involving iron and magnesium are neglected as no cations or anions are included in solution, where is it considered less important than the other chemical production terms (Angle et al. (2021)) and would require a significant upgrade to the aqueous phase chemistry component, which is not the focus of this work. The subsequent change in the gas phase for SO_2, NH_3, O_3, H_2O_2, SO_4^{2-} and NH_4^+ is then accounted for once the oxidation step has occurred.

In-cloud and below-cloud scavenging of SO_2 and NH_3 is also affected by acidity of cloud and rain water, through use of an effective Henry solubility following Seinfeld and Pandis (2006) using a fixed value of pH. Until CY47R3 this value was set to

pH of 5.5 globally. In CY48R1, this has been updated towards pH of 5.6 (over ocean) and pH of 5 (over land). In CY49R1, the diagnostic precipitation pH as provided by EQSAM4Clim is used to compute the effective Henry solubility of SO_2 and NH_3.

210 The impact of the use of updated cloud acidity in aqueous chemistry and rain acidity in the IFS-COMPO wet deposition is found to be small in general, and smaller than the impact of other contributions and in particular of the changes in gas/particle partitioning brought by the use of EQSAM4Clim. Hence, no specific discussion of this has been included, as we chose to focus on model upgrades that have the largest impact on simulated fields.

2.3 Other IFS-COMPO updates included in CY49R1

215 In this subsection we describe additional aerosol modeling changes implemented in cycle 49R1, which also affect the results of CY49R1 model simulations presented in Section 3 as compared to the default CY48R1 configuration. These updates are described in less detail than the implementation of EQSAM4Clim; for an exhaustive description we refer the reader to the future operational cycle 49R1 documentation which will be released simultaneously with the operational implementation of cycle 49R1.

2.3.1 Updates to wet deposition

220

In CY48R1, the aerosol and chemistry wet deposition routines of IFS-COMPO are distinct, but both include a scheme adapted from Luo et al. (2019) which is used operationally. In order to ensure a consistent approach between aerosol and trace gases wet deposition, and to facilitate the code maintenance, the various implementations of the native chemistry and aerosol wet deposition routine have been merged into a single routine that is used to represent the wet deposition processes for both aerosols

225 and chemical species. This new routine is called with either the chemical tracers or aerosol tracers as an input. Similarly to CY48R1 and before, it is called twice with input from the large scale and convective precipitations. In the convective precipitation case, the assumed precipitation fraction has been harmonised to a value of 0.05 (0.1 was used for chemistry scavenging, 0.05 for aerosol scavenging). The following upgrades have additionally been included for aerosol wet deposition:

– Implementation of the aerosol activation parameterization of Verheggen et al. (2007). The authors provide an estimate of
230 the fraction of aerosols that can be scavenged through in-cloud processes as a function of temperature. This parameterization is used in mixed clouds, i.e. for temperatures below the freezing point and above 233K. For temperatures above 0°C, the consistency of the parameters that determine the fraction of aerosols that are subject to in-cloud wet deposition with the results of the Verheggen parameterization has been verified.

– For below-cloud scavenging of aerosol species, the scavenging rates have been updated to follow more closely the
235 particle size dependency of Croft et al. (2009). This involved updating the below cloud scavenging parameters of the table file (for rain and snow), depending on the species and the assumed size distribution, as well as implementing a below-cloud scavenging rate that is dependent on rain/snow intensity. This results in a significant increase in simulated below-cloud scavenging, which is consistent with results of Croft et al. (2009).

Both aerosol and chemistry wet deposition use the re-evaporation scheme from de Bruine et al. (2018).
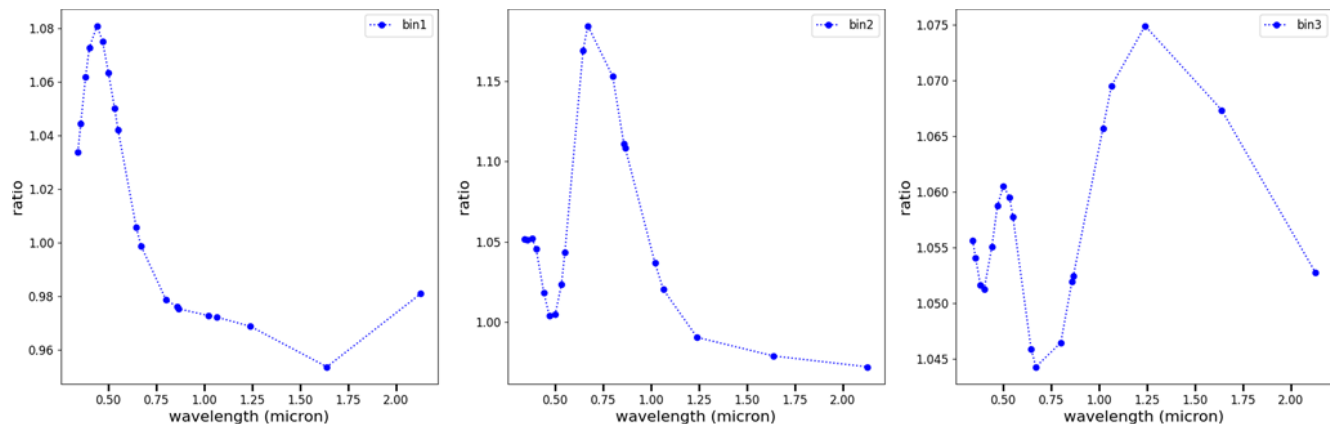
Figure 2. Ratio of non-spherical vs spherical dust mass extinction as a function of wavelength, for each of the IFS three dust bins.

2.3.2 Updates to desert dust

In CY49R1, hydrophilic growth for dust has been introduced, following Chen et al. (2020), using a growth factor that increases linearly from 0.8% at 10% RH to 7.4% at 95% RH. The hydrophilic growth is used in the desert dust optical properties, as well as in dry deposition. It is well know that desert dust are composed of mineralogical components and aggregates with very different shapes, which means that the assumed spherical shape of dust used in the Mie code (Wiscombe, 1980) that computes offline the aerosol optical properties (mass extinction, asymmetry parameter, single scattering albedo and lidar ratio) is clearly invalid. Using the online tool MOP-SMAP (Gasteiger and Wiegner, 2018), a scaling factor that accounts for the effect of asphericity has been computed, which is applied on the spherical desert dust optical properties computed with the Mie code. The assumed shape of the desert dust particles is derived from Kandler et al. (2009): a prolate spheroïd with an aspect ratio of 1.6. The ratio of non-spherical vs spherical dust mass extinction as a function of wavelength is shown in Figure 2 for each of the 3 dust bins. The implementation of non-spherical dust in cycle 49R1 leads to an increase in the dust mass extinction of an increase of 5-20% in the ultraviolet and visible part of the spectrum for the fine and coarse bins, and of 5-10% for the super coarse bin

2.3.3 Updates to sea-salt aerosol

Since CY47R1, the sea-salt aerosol emissions are computed from the simulated whitecap fraction following Monahan et al. (1986), and the whitecap fraction is estimated from the surface wind speed and sea-surface temperature using the approach of Anguelova and Webster (2006), as detailed in Rémy et al. (2022). However, the Monahan et al. (1986) parameterization is applicable to particles between 0.8 and 8 μm diameter, which means that a large fraction of the coarsest sea-salt aerosol bin is outside of the applicability range of this parameterization. Following the results of Remy and Anguelova (2021), the sea-spray size distribution of Gong (2003) has been implemented to compute sea-salt aerosol emissions from the whitecap fraction. The

9

computation of the whitecap fraction itself is unchanged as compared to CY47R1 and CY48R1 and uses the Albert et al. (2016) formulation. The flux of emitted sea-salt aerosols is expressed as a function of whitecap fraction W, particle size D_p as :

$$\frac{dF}{dD_p} = W \times 3.5755 \times 10^5 D_p^{-A} (1 + 0.057 D_p^{3.45}) \times 10^{1.607 \exp(-B^2)} \tag{1}$$

where

$$A = 4.7(1 + \theta D_p)^{-0.017 D_p^{-1.44}}$$
$$B = \frac{0.433 - \log(D_p)}{0.433} \tag{2}$$

Here, θ is an adjustable parameter, which (Gong, 2003) introduced to fit the SSSF values to field observations of O'Dowd et al. (1997).

2.3.4 Update of the PM formulae

Particulate Matter smaller than 1, 2.5 and 10 μm are important outputs of IFS-COMPO. In CY49R1, the assumed size distribution used to compute these diagnostic outputs have been updated so as to be consistent with the one assumed in the aerosol optics. This results in signficantly higher PM1 and PM2.5, and has a small impact on PM10. PM1, 2.5 and 10 are computed with the following formulae that uses the surface mass mixing ratio from each aerosol tracer as an input, denoted $[SS_{1,2,3}]$ for sea-salt aerosol, $[DD_{1,2,3}]$ for desert dust, $[NI_{1,2}]$ for nitrate, $[OM], [BC], [SU], [AM], [SOA]$ for Organic Matter, Black Carbon, Sulfate, Nitrate, Ammonium and SOA respectively :

$$PM_1 = \rho\Big(\frac{[SS_1]}{4.3} + 0.5[DD_1] + 0.96[OM] + 0.96[BC] + 0.91[SU] + 0.91[NI_1] + 0.91[AM] + 0.96[SOA]\Big)$$

$$PM_{2.5} = \rho\Big(\frac{[SS_1]}{4.3} + 0.6\frac{[SS_2]}{4.3} + [DD_1] + 0.15[DD_2] + [OM] + [BC] + [SU] + [NI_1] + 0.5[NI_2] + [AM] + [SOA]\Big)$$

$$PM_{10} = \rho\Big(\frac{[SS_1]}{4.3} + \frac{[SS_2]}{4.3} + 0.05\frac{[SS_3]}{4.3} + [DD_1] + [DD_2] + 0.4[DD_3] + [OM] + [BC] + [SU] + [NI_1] + [NI_2] + [AM] + [SOA]\Big)$$

where ρ is the air density at surface. The sea-salt aerosol tracers are divided by 4.3 so as to transform the mass mixing ratio at 80% ambient relative humidity to dry mass mixing ratio.

2.3.5 Update of the aerosol optics

The aerosol optical properties (mass extinction, single scattering albedo and asymmetry parameter) are computed offline using a Mie code, as described in ECMWF (2023). The assumed size distribution used for the sulphate optical properties has been updated, with a modal radius increase from 0.0355 to 0.11 micron, and a geometric standard deviation decrease from 2 to 1.6. Also, a 1.375 scaling factor that was applied to sulphate mass extinction in previous cycles, which accounted for the difference in molar mass between ammonium sulphate and sulphate, has been removed in cycle 49R1, as ammonium is represented as a specific tracer with its own optics. This led to a significant decrease in the sulphate mass extinction in cycle 49R1.

3 Experimental set-up and observations

3.1 Experiments

In this work we consider three cycling forecasts experiments without data assimilation, denoted CY48R1, CY49R1 and CY49R1_NOE4C. The experiments simulated the period from 1/12/2018 to 31/12/2019, with December 2018 used as a spin-up period. Similarly, three similar experiments, which we will refer by the same names, have simulaed the period from 1/12/2016 to 31/12/2017, in order to evaluate them against observations not available in 2019. The resolution used is the current operational resolution of T_L511 with 137 vertical levels. CY48R1 uses a configuration similar to that of the operational CY48R1, while CY49R1 integrates all chemistry and aerosol modeling updates of IFS-COMPO intended for the operational CY49R1, including the use of EQSAM4Clim and its coupling to tropospheric chemistry processes, but otherwise using a version of the meteorological core of IFS-COMPO identical to the CY48R1 experiment. This means that the differences between the two experiments come only from atmospheric composition modeling updates, and not from changes from the meteorological part of the IFS, or changes in the emissions. The 49R1_NOE4C experiment deactivates the use of EQSAM4Clim, and reverts to application of the equilibrium model available in CY48R1 (Rémy et al., 2022). All experiments use the same emissions: anthropogenic emissions from the CAMS_GLOB_ANT v5.3 dataset (Soulie et al., 2023), biomass burning emissions from the Global Fire Assimilation System version 1.4 (GFAS, Kaiser et al. (2012)), aviation emissions from CAMS-GLOB-AIR v1.1, biogenic emissions from a climatology constructed from the CAMS-GLOB-BIO v3.1 inventory and natural emissions of DMS over the ocean from CAMS-GLOB-OCE v3.1. All of the experiments use only the tropospheric chemistry component of IFS-COMPO; no explicit stratospheric chemistry is included, as used operationally in CAMS. All simulations are run without data assimilation, so as to better assess the impact of modelling changes.

4 Comparison of budgets and model fields

4.1 Changes in global surface concentrations

Figure 3 and 4shows the mean annual global surface concentrations for 2019 from CY48R1 for SO_4^{2-}, HNO_3, NO_3^-, NH_3 and NH_4^+, along with the absolute differences when compared to the other simulations. In general the most significant changes in precursors and particles occur between 50°N-50°S, especially over India and South-East Asia, where high fluxes of the primary emissions of NO_x, NH_3 and SO_2 occur. For SO_4^{2-} moderate increases occur over land, which are somewhat moderated by the application of EQSAM4Clim. This increase is likely associated with the reduced wet deposition in mixed clouds in the two CY49R1 simulations. Significant increases in HNO_3 occur with associated decreases in NO_3^- in CY49R1, while in CY49R14C, surface NO_3^- is decreased as compared to CY48R1, but to a lesser extent than with CY49, and HNO_3 is little impacted. The lower NO_3^- in CY49R1_NOE4C is likely caused by the higher sulfate, which prevents the formation of nitrate. The additional decrease of surface NO_3^- with CY49R1 as compared to CY49R14C is caused by the use of EQSAM4Clim, which tilts gas/particle partitioning more towards the gas phase. Similar but smaller changes occur for NH_3 and NH_4^+.
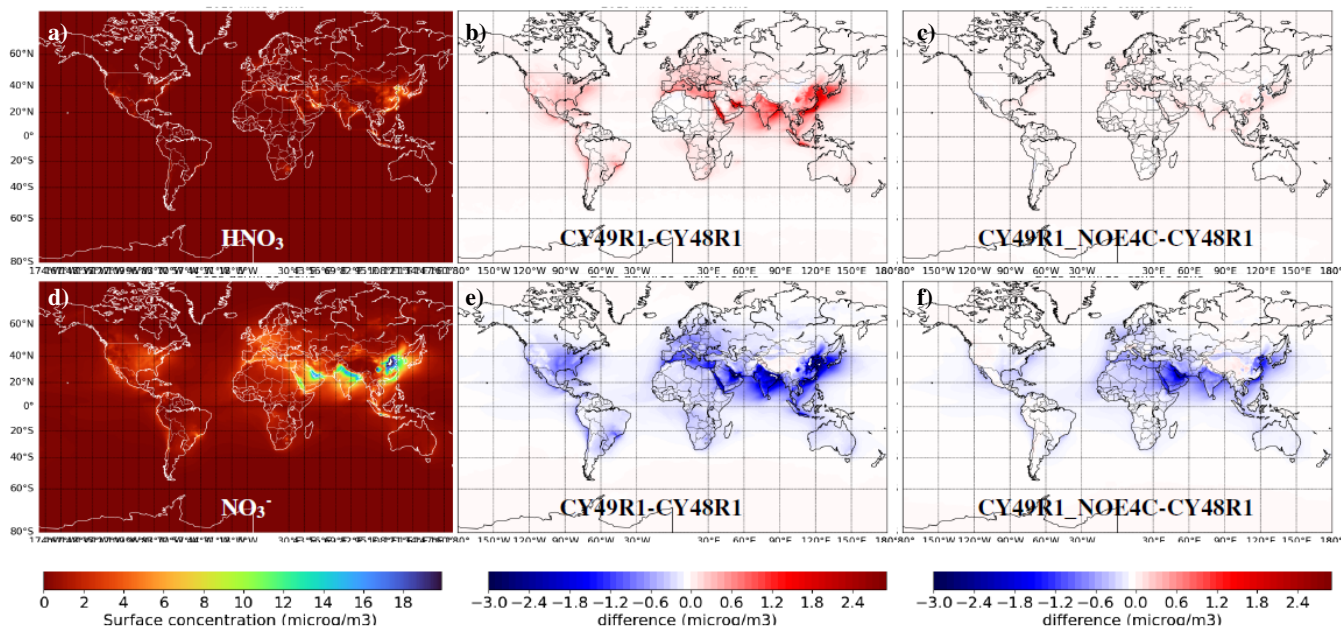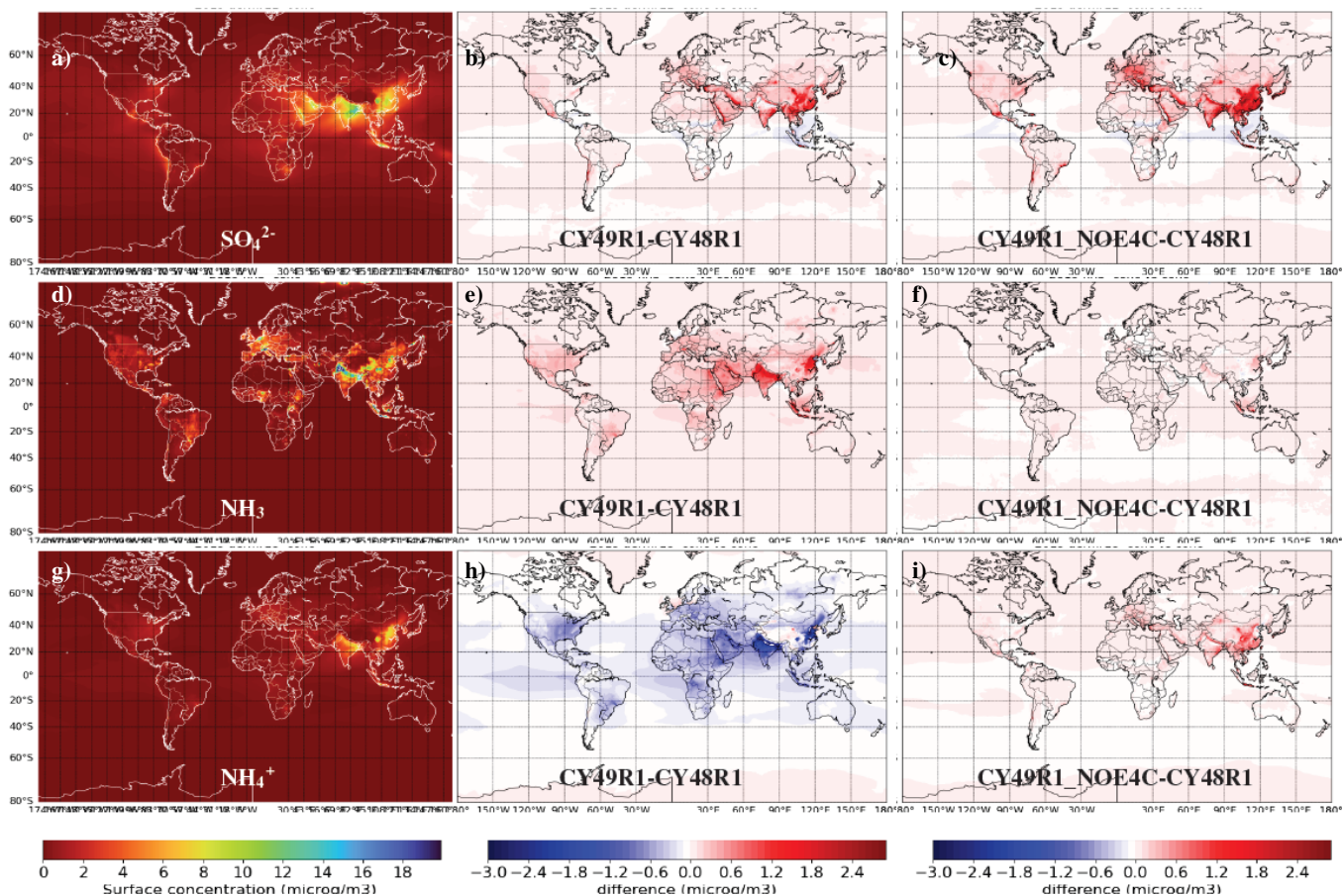
Figure 3. Left (panels a and d): Annually averaged surface concentrations of HNO_3 (top) and NO_3^- (bottom) as simulated by CY48R1. Middle (panels b and e) and right (panels c and f), difference CY49R1 minus CY48R1 and CY49R1_NOE4C minus CY48R1. Units are in $\mu g/m^3$.

4.2 Global chemical budgets for presursors and particles

Table 1 shows the chemical budget terms of the key species involved in the S and N cycles in IFS-COMPO for 2019 for
320 both gas-phase species and particulates. The SO_2 sources are from direct primary anthropogenic emissions with a contribution (30%) from the oxidation of Dimethyl Sulphide by OH and outgassing/volcanic eruptions. The SO_2 emissions from explosive eruptions such as that of the Raikoke on 21-25 of June 2019, are not taken into account. From Table 1 it can be seen that the SO_4^{2-} production increases by 5-6% (around 2.4 Tg yr^{-1}) in CY49R1_NOE4C compared to CY48R1, with a corresponding small reduction in the global burden of SO_2. The tropospheric lifetime of SO_2 is also decreased by 10% to 2.4 days with an
325 associated increase in lifetime of 25% for SO_4^{2-} to 4.4 days, potentially affecting AOD near strong source regions. Lifetimes of SO_x species are relatively unaffected by the application of EQSAM4Clim. The lifetime of SO_2 exhibits strong seasonality (not shown). Satellite derived estimates are reported between 10-20 hours during summertime, to 40-60 hours during wintertime in the boundary layer(Lee et al., 2011);(Qu et al., 2019). The simulated value is at the upper limit of these values, which can be explained by the fact that this is a global average over the whole atmosphere, so including areas where dry and wet oxidation
330 processes are much slower. For SO_4^{2-}, the corresponding estimated lifetime is around 4-5 days (Chin et al. (1996);van Noije et al. (2014)), agreeing well with our results.

For HNO_3 only minimal changes in the tropospheric budget occur between CY48R1 and CY49R1_NOE4C, with the dry and wet deposition terms exhibiting only limited differences due to the updated deposition routines. With the activation of

Figure 4. Left (panels a,d and g): Annually averaged surface concentrations of SO_4^{2-}, NH_3 and NH_4^+ (from top to bottom) as simulated by CY48R1. Middle (panels b, e, and h) and right (panels c, f and i), difference CY49R1 minus CY48R1 and CY49R1_NOE4C minus CY48R1. Units are in $\mu g/m^3$.

EQSAM4Clim, the tropospheric burden of HNO_3 almost doubles, mainly due to a reduced fraction of HNO_3 being converted
335   into NO_3_1 (from gas-to-particle partitioning). The parameterization of heterogeneous production of nitrate particles on top of
sea-salt and dust particles in EQSAM4Clim is strongly suppressed, leading to a much smaller burden of NO_3_2 with CY49R1
as compared to CY49R1_NOE4C, and contributing to the higher burden of HNO_3 for this experiment. Compared to CY48R1,
for CY49R1_NOE4C there is only a small repartitioning of nitrate from NO_3_1 towards NO_3_2. This is associated to a lower
NO_3_1 production, caused by a higher SO_4^{2-} aerosol burden, which in turn results mainly from the wet deposition updates.
340   For CY49R1, the total burden of NO_3^- decreases by around 50% compared to CY48R1. This is particularly attributed to the
change in burden of NO_3_2, as the burden of NO_3_1 increases by more than 50%. The use of EQSAM4Clim increases the
tropospheric lifetime of NO_3_1 from 4.9 days up to 6.2 days, whilst reducing the lifetime of NO_3_2 by 1.2 days. This essentially
shifts simulated nitrate particles towards small sizes.

Table 1. Global chemical budget terms for 2019 of SO_2, SO_4^{2-}, NO_3^- aerosol from gas/particle partitioning (NO_3_1) and from heterogeneous reactions (NO_3_2), HNO_3, NH_3 and NH_4^+ as simulated by the three experiments CY48R1, CY49R1 and CY49R1_NOE4C. Fluxes are expressed in TgS yr^{-1} or TgN yr^{-1} and burden in TgS or TgN, respectively. For HNO_3, NO_3_1 and NO_3_2 no direct emission occurs and for NH_3 no chemical production term exists. Results are presented as CY48R1 / CY49R1 / CY49R1_NOE4C

species	emissions+production	dry deposition	wet deposition	burden	lifetime (days)
SO_2	77.4 / 77.4 / 77.4	22.1 / 21.7 / 20.8	8.7 / 6.6 / 7.6	0.39 / 0.37 /0.35	2.7 / 2.5 / 2.4
SO_4	46.6 / 49.2 / 49.0	5.5 / 5.4 / 5.3	41.1 / 43.8 / 43.7	0.44 / 0.59 / 0.59	3.4 / 4.4 / 4.4
HNO_3	45.8 / 47.3 / 46.1	4.6 / 12.2 / 5.6	15.7 / 22.0 / 13.9	0.15 / 0.29 / 0.14	1.2 / 2.2 / 1.1
NO_3_1	3.5 / 4.7 / 2.9	1.0 / 0.63 / 0.79	2.5 / 4.1 / 2.1	0.05 / 0.08 / 0.04	4.7 / 6.2 / 4.9
NO_3_2	22 / 8.4 / 23.7	6.7 / 5.4 /11.4	15.3 / 3.0 /12.3	0.20 / 0.06 / 0.25	3.3 / 2.6 / 3.8
NH_3	56.4 / 53.2 / 55.8	17.1 / 23.2 / 17.5	9.7 / 12.5 / 8.1	0.13 / 0.28 / 0.16	0.84 / 1.9 / 1.04
NH_4	29.6 / 17.5 / 30.2	4.7 / 1.7 / 4.7	24.8 / 15.6 /25.5	0.28 / 0.19 /0.39	3.4 / 4.0 / 4.7

For the conversion of NH_3 to NH_4^+, the updates in CY49R1_NOE4C, reduces the wet deposition term for NH_3 by around 15% increasing both the burden and lifetime. This subsequently increases the NH_4^+ burden and lifetime by around 30%. The use of EQSAM4Clim in CY49R1 increase further the burden and lifetime of NH_3, associated with increased dry and wet deposition. Similarly to the HNO_3/NO_3^- couple, EQSAM4Clim tilts the gas/particle conversion towards the gas phase for the NH_3/NH_4^+ couple, leading to substantially lower NH_4^+ production, burden and deposition with CY49R1 as compared to CY49R1_NOE4C, and correspondingly, a higher simulated burden and deposition of NH_3. This results in a lifetime of NH_3 of 1.9 days with CY49R1, which is more than twice the value with CY48R1 (0.84 days). This is also at the high end of values found in Luo et al. (2022) from GEOS-CHEM, which range from less than 10 hours lifetime over China and Northern high latitudes up to more than 40 hours over large parts of Africa and Australia. (Van Damme et al., 2018), provides a figure of 12 hours but close to specific emission sources. The discrepancy between this short lifetime value and the CY49R1 1.9 day lifetime can be explained by different scales (global versus local) and the fact that the longer lifetimes are mostly far away from NH_3 sources.

5 Evaluation

5.1 Evaluation of simulated PM2.5

Both PM2.5 and PM10 surface observations are provided by the AirNow database (https://www.airnow.gov/about-airnow/, last access: 7 July 2023) covering U.S., the European Environment Agency (EEA) covering Europe and the China National Environmental Monitoring Center covering China. For these three regions, special care was taken to use only the rural background stations representative of locations away from strong point sources.

Table 2. Regional evaluation of simulated daily PM2.5 as compared against background rural stations for each region. The Modified Normalized Mean Bias (MNMB), Fractional Gross Error (FGE) and the Pearson correlation coefficient (R) are given, where the colours denote CY48R1 / CY49R1 / CY49R1_NOE4C. The best values are highlighted in bold. Values for the MNMB are given in $\mu g/m^3$. The number of background rural stations for each region is indicated in parentheses.

Skill scores	N. America (124)	Europe (69)	China (153)
MNMB	-0.23 / **-0.03** / 0.2	**-0.06** / 0.13 / 0.29	-0.16 / **0.12** / 0.24
FGE	0.55 / **0.51** / 0.55	0.5 / **0.49** / 0.52	0.49 / **0.47** / 0.53
R	0.42 / **0.43** / 0.42	0.59 / **0.67** / 0.66	0.53 / **0.61** / 0.55

The 2019 annual mean global distribution of simulated PM2.5 are shown in Figure 3, along with the absolute differences between CY49R1_NOE4C and CY49R1 as compared against CY48R1. The highest PM2.5 concentrations occur over Africa/Middle East (associated with desert dust) and India/China (associated with anthropogenic particles), which are 3-7 times higher than the PM2.5 concentrations simulated for U.S., Europe, Russia and South America. Signatures over the ocean occur related to sea-salt aerosol, resulting in background PM2.5 concentrations of around 20 $\mu g/m^3$. Considering the differences of CY49R1_NOE4C compared against CY48R1, there is a moderate reduction in PM2.5 over the pristine ocean of between 2-4 $\mu g/m^3$ related to the application of an updated approach for sea-salt emissions, in contrast to an increase over land of up to 4-15 $\mu g/m^3$ over most regions. For North Africa, technical changes to the wind gusts used in the emission scheme led to a decrease in desert dust emissions, therefore reducing the PM2.5 concentrations. The largest increases occur for regions with high anthropogenic emissions, reaching 12-18 $\mu g/m^3$ for India and East Asia, thus 25% in relative terms. These changes are reduced by the application of EQSAM4Clim, over e.g. U.S. and Europe, related to the significant reduction in the simulated surface concentration of NH_4^+ and NO_{3_2} (see Table 1).

Figure 6 shows the weekly variability in PM2.5 as seen in the regional composites of observed and simulated particle concentrations for Europe, U.S. and China, for background rural sites. The associated Fractional Gross Error (FGE) between simulations and observations is shown in the right column, providing some estimate as to the ability of IFS-COMPO in capturing the observations. No real seasonal cycle exists in the regional mean PM2.5 concentrations in U.S., whereas for China a strong seasonal cycle in PM2.5 exists with maximal concentrations during wintertime and, with a weaker amplitude, also in Europe. Figure 6 is complemented by Table 2 which provides the 2019 average of the Modified Normalized Mean Bias (MNMB), the FGE and the correlation coefficient of simulated PM and AOD versus observations.

For CY48R1, a strong negative bias occurs during wintertime for China and Europe, indicating muted particle formation during colder periods with shorter days, with FGE values of between 0.6-0.8. For the summertime, biases are typically lower with FGE values of between 0.3-0.4 across regions. The updates of CY49R1_NOE4C reduce the wintertime FGE to between 0.3-0.4, substantially reducing the simulated bias and improving on the representation of weekly variability in PM2.5. The correlation between simulated and observed values is significantly higher with CY49R1 over China and Europe, as shown in Table 2. In contrast, during summertime the FGE increases to 0.5-0.7 across all regions with CY49R1_NOE4C, somewhat

degrading the performance of IFS-COMPO compared to CY48R1. The use of EQSAM4Clim in CY49R1 provides the best compromise between the other simulations, in that the wintertime improvements occur in tandem with lower summertime biases which are comparable to CY48R1 for Europe and slightly higher for U.S. and China.

5.2 Evaluation of AOD at 500 and 550nm

In this section, we use Aerosol Optical Depth (AOD) at 500nm observations, which are taken from the Aerosol Robotic Network (AERONET; Holben et al. (1998)) to validate the integrated column properties of the simulations. In this study AERONET level 2 data are used for evaluation, which are cloud screened and quality assured with final calibrations, in preference to the level 1.5 AOD data at 500 nm. We also use the corresponding Ångström exponent values derived from AERONET data evaluated between 440-865nm. The $1° \times 1°$ gridded monthly merged AOD at 550nm product provided by FMI (Sogacheva et al., 2020) has also been used to evaluate simulated AOD, particularly over regions where fewer AERONET stations are available.

The updates of the tropospheric aerosols in IFS-COMPO CY49R1 bring significant changes in the mean simulated AOD at 550nm, as shown in Figure 7. In general, the simulated AOD shows increases in the range 0.04-0.1 AOD units in CY49R1, except over regions which are significantly affected by desert dust. For these dry regions decreases in AOD occur of between 0-0.06 AOD units. Such decreases can be attributed to changes in the inputs used in the dust emission scheme, which lead to lower dust emissions in general. The largest increases in AOD occur over India and China corresponding to the regions exhibiting significant increases in PM2.5 (see. Fig. 5). Over oceans, the increases in AOD are mostly caused by the changes in the emissions of sea-salt aerosol, with the implementation of the Gong (2003) sea-spray size distribution. At the higher latitudes the increase of the simulated AOD with the CY49R1 simulations as compared to CY48R1 is even more significant compared to the low values, and is caused by the reduction in wet deposition in mixed and ice clouds following the implementation of the Verheggen et al. (2007) aerosol activation parameterization in the wet deposition scheme.

Comparing the simulated AOD at 550nm by the CY48R1 and CY49R1 experiments that have simulated 2017 with the values from the FMI merged AOD product (Sogacheva et al. (2020)) shows a relatively good agreement (Figure 8). Over oceans, the simulated values are generally too low with CY48R1, and often too high with CY49R1; the difference is caused by updates in the sea-salt aerosol emissions. Over regions with high anthropogenic emissions, the AOD is on average simulated too low over Europe and India, and too high over Eastern U.S. and China with CY48R1. Over Eastern U.S., this overestimation is caused mainly by too high biogenic secondary organics and sulphate (not shown). CY49R1 brings a small decrease in simulated AOD over China and India, and an increase over Europe and Eastern U.S., thereby reducing bias over Europe and China, and increasing it over Eastern U.S. and India. Figure 8 also shows the corresponding Fractional Gross Error (FGE) averaged over 2017 of monthly simulated vs retrieved AOD at 550nm. Over most of areas, the FGE is significantly improved by CY49R1 as compared to CY48R1. However, some degradation is noted over parts of oceans and over Eastern U.S, due to too high AOD values.

Generally, there is an increase in simulated AOD in both CY49R1_NOE4C and CY49R1 experiments, as shown by the comparison against AERONET observations in Figure 9. Figure 9 is complemented by Table 3, which also provides global and

16

Table 3. Regional evaluation of simulated daily AOD at 500nm as compared against AERONET level 2 for AOD. The Modified Normalized Mean Bias (MNMB), Fractional Gross Error (FGE) and the Pearson correlation coefficient (R) are given, where the colours denote CY48R1 / CY49R1 / CY49R1_NOE4C. The best values are highlighted in bold. Values for the MNMB are given in AOD unit. The mean number of AERONET stations for each region is shown in parentheses

Skill score	Global (461)	N. America (162)	Europe (113)	China (23)	Africa (64)
MNMB	-0.24 / **0.04** / 0.06	-0.28 / **0.09** / 0.14	-0.29 / -0.06 / **0.0**	-0.15 / 0.12 / **0.11**	**0.06** / 0.14 / 0.14
FGE	0.53 / **0.43** / 0.44	0.53 / **0.41** / 0.42	0.44 / 0.34 / **0.32**	0.49 / **0.44** / 0.45	0.42 / **0.38** / **0.38**
R	0.79 / **0.80** / **0.80**	**0.74** / 0.73 / **0.74**	0.73 / 0.76 / **0.77**	0.72 / **0.74** / 0.72	0.75 / 0.78 / **0.79**

regional skill scores (MNMB, FGE and correlation coefficient). For CY48R1 a significant low bias of -0.02 to -0.1 AOD units occur for the global mean values and for Europe, U.S., India and China. With the exception of the U.S., the summertime AOD bias is generally smaller. Over Africa seasonal variability is low in the observed AOD values, where no clear bias exists in CY48R1. For both CY49R1_NOE4C and CY49R1 large increases in AOD (between 0.025 and 0.1 AOD unit) can be seen as compared to CY48R1 over all regions, with a quite constant increase of 0.05 averaged globally. For more polluted regions (e.g. Europe and China) this results in a clear improvement during wintertime in the simulated bias at 500nm. For the U.S. a positive bias in AOD is introduced throughout the year and for China the positive bias enhanced during summertime. Over Africa, both CY49R1 experiments bring a small positive bias on average. The difference between CY49R1_NOE4C and CY49R1 is generally small for the AOD at 550nm, except in summertime over Europe, China and N. America, with simulated AOD at 550nm values lower by -0.02 to -0.05 AOD unit of CY49R1_NOE4C. Overall, as indicated by Figure 9 and Table 3 CY49R1 brings an improvement as compared to CY48R1 globally and for all regions in terms of FGE, and for all regions but Africa for MNMB. The impact on correlation is small but positive in general, except over North America.

5.3 Evaluation of the Ångström exponent

The evaluation of the weekly Ångström exponent (AE) between 440-865nm, when compared to AERONET values is shown in Figure 10. The simulated AE decreases by around 0.1 in CY49R1_NOE4C and CY49R1 at global scale, indicating that the relative amount of simulated coarse particles increases as compared to the finer particles. This results from the several updates introduced into CY49R1: the change and decrease in AOD from SO_4^{2-} , and the increase in contribution to AOD by sea-salt. With the exception of Europe, this decrease in the simulated AE leads to an improvement via lower biases as compared to CY48R1, indicating an over-estimate in the abundance of fine particles. There is a significant change in the distribution with respect to particle size in both CY49R1_NOE4C and CY49R1. Over Europe, a negative bias of 0.2-0.3 exists in both CY49R1 and CY49R1_NOE4C. For U.S., China and India, a positive bias of 0.2-0.4 exists in CY48R1, with a reduction of between 0.1-0.2 for CY49R1_NOE4C and CY49R1. Over Africa the changes are limited: the general decrease in simulated AE with the two CY49R1 simulations is counterbalanced by the decrease in simulated abundance of desert dust aerosols. In general, the

17

simulated AE in CY49R1_NOE4C is quite similar to that simulated in CY49R1, showing that the application of EQSAM4Clim only has a second-order effect on the simulated Angström exponent.

5.4 Evaluation of surface concentrations

Observations of speciated aerosol surface concentrations from three datasets have been used: the Clean Air Status and Trends Network (CASTNET; https://www.epa.gov/castnet, last access: 27 June 2023) for the US, the European Monitoring and Evaluation Programme (EMEP, https://ebas.nilu.no/, last access: 21 July 2023) for Europe and the Acid Deposition Monitoring Network in East Asia (EANET, https://www.eanet.asia/, last access: 12 July 2023). The CASTNET network is operated by the U.S. Environmental Protection Agency (EPA). The ambient concentrations of gases and particles are collected with an open-face three-stage filter pack at the measurement sites and a three-stage filter pack or bulk samplers at EMEP and EANET sites. For our study we choose weekly ambient concentrations of HNO_3, SO_4^{2-}, NO_3^- and NH_4^+, which are available from 93 of the CASTNET sites in 2019.

The Ammonia Monitoring Network (AMoN, https://nadp.slh.wisc.edu/networks/ammonia-monitoring-network/, last access on 25 July 2023) also provides three-daily observations of surface NH_3 for 107 sites in the U.S. . Daily observations of ambient concentrations of selected trace gases and aerosol species, including HNO_3, SO_4^{2-}, NO_3^-, NH_3 and NH_4^+, are available from 27 to 31 EMEP stations depending on the species. For EANET, only yearly average concentrations of SO_4^{2-}, NO_3^- and NH_4^+ have been used, over 41 stations.

Comparisons of the temporal distribution of precursor and associated particulate concentrations made against the observational surface networks show varying degrees of improvement depending on the particle type, where Table 4 provides the Mean Bias (MB), root-mean square error (RMSE) and Pearsons correlation coefficients (R) for 2019. The frequency of the measurements varies across regions, meaning that statistics for e.g. Europe (EMEP) are more robust using daily values than for East Asia (EANET) which only provide annual values limited to a handful of stations without corresponding precursor measurements thus limiting the analysis for this region. In this subsection we focus on oxidized and reduced nitrogen species in the gas and particulate phase, because they are the species that exhibit the largest impact from the cycle 49R1 updates and the use of EQSAM4Clim in particular. Sulfate is also shown, but SO_2 is not, as there are relatively little differences between the three experiments.

For HNO_3 and NO_3^-, density scatterplots for the comparisons against weekly aggregated CASTNET surface observations for 2019 are shown as separate panels in Figure 11 for the three simulations. For CY48R1, a small negative MB exists for HNO_3 in CY48R1, with a poor correlation with the observations. The associated MB for NO_3^- is large and positive, again with a poor correlation (R=0.31), indicating an over-estimation in NO_3^- formation. Comparing CY49R1_NOE4C shows only small reductions in the MB occur with a further decrease in R, showing that the cycle 49R1 updated other than the use of EQSAM4Clim have a small impact for this species. The application of EQSAM4Clim in CY49R1 significantly reduces NO_3^- formation (see Table 1), which shifts the equilibrium towards the gaseous precursor HNO_3, and for U.S. subsequently increases the MB and RMSE values albeit with a much improved correlation indicating a too long lifetime under a similar production term (c.f. Table 1). For NO_3^- there is a significant reduction in the simulated mean bias and error, with a corresponding large

18

increase in correlation, which generally improves continental particle distributions and the resulting PM2.5 comparisons as shown in Fig. 6. Therefore, the use of EQSAM4Clim in cycle 49R1 results in an improvement in the ability of IFS-COMPO towards forecasting resident NO_3^- concentrations.

The corresponding density scatter plots for the comparisons of NH_3 and NH_4^+ against AMoN/CASTNET data are shown in Figure 12. As for HNO_3, small negative mean bias values exist for NH_3 in CY48R1, with an associated weak correlation (R=0.36). For NH_4^+ a moderate MB exits indicating an over-estimate in particle formation similar to NO_3^-. The application of EQSAM4Clim in CY49R1 results in significant improvements in both the MB and RMSE of simulated surface NH_4^+ across U.S. with a general reduction in the efficacy of particle formation, as would be expected considering the improvements in the NO_3^- comparisons. Again, this helps improve on any PM2.5 forecast bias in IFS-COMPO. The impact of the use of EQSAM4Clim on simulated surface concentration of NH_3 is smaller than the impact noticed for NH_4^+ but still positive, with an improvement of R from 0.36 with CY48R1 and CY49R1_NOE4C to 0.4 with CY49R1.

Figure 13 focuses on a comparison of simulated and observed surface concentrations for both precursors and particles for a single CASTNET/AMoN measurement station, namely: Mackville in Kentucky (Lat : 37.75°N , Lon : 85.07°W). The change in the equilibrium position of gas-particle partitioning for the HNO_3/NO_3^- couple towards less particles and more of the gas phase precursor becomes apparent when EQSAM4Clim is used, leading to a significant improvement in the representation of surface NO_3^-, with an associated increase in the relatively low bias simulated for HNO_3 in CY48R1 and CY49R1_NOE4C to a high positive bias with CY49R1. Although the measured surface HNO_3 remains relatively constant throughout the year between 0.5-1$\mu g/m^3$, a strong seasonal cycle exists for surface NO_3^-, where colder conditions increase the particle stability under lower water vapour concentrations increasing resident concentrations two- to three-fold. This monthly variability is captured well by CY49R1. The same phenomenon occurs with to a lesser extent for the NH_3/NH_4^+ couple, again with a notable improvement in the simulated surface concentration of NH_4^+ by CY49R1 as compared to the other two simulations. For NH_3 the observed seasonal cycle is missed across simulations, with a maxima simulated in spring and observed in summer. The timing in the simulations is strongly governed by the monthly variability and magnitude in the emission inventories, which have been show to have significant difference when compared to satellite derived emission estimates (Cao et al. (2022)). For NH_4^+ the excessive particle concentrations simulated in CY48R1 and CY49R1_NOE4C during summertime (+200% bias) significantly improves upon the application of EQSAM4Clim.

Table 4 summarizes the evaluation of the simulated surface concentrations of selected species against observations over Europe, U.S. and East Asia. This evaluation confirms the conclusion reached using only the CASTNET/AMoN networks, showing a clear improvement for all networks of simulated surface concentration of NO_3^- and NH_4^+ in terms of bias, RMSE and correlation coefficient. For example, the RMSE of simulated daily NO_3^- as compared to EMEP observations over Europe decreases from 3.55 to 2.71 $\mu g/m^3$ by CY49R1_NOE4C as compared to CY48R1, and that of yearly NO_3^- as compared to EANET observations over East Asia from 4.25 to 1.47 $\mu g/m^3$. For HNO_3 and SO_4^{2-}, the skill scores of the CY49R1 experiments are more mixed.

Table 4. Regional evaluation of simulated surface concentrations of selected aerosol and trace gases species associated with particle production. The Mean Bias (MB), Root Mean Square Error (RMSE) and the Pearson correlation coefficient (R) are given, where the colours denote CY48R1 / CY49R1 / CY49R1_NOE4C. The best values are highlighted in bold. Values for the MB are given in $\mu g/m^3$. The evaluation is carried out against weekly values for CASTNET, three-daily values for AMoN, daily values for EMEP and yearly values for EANET.

species		U.S. (CASTNET/AMoN)	Europe (EMEP)	East Asia (EANET)
SO_4^{2-}	mean Bias	**0.41** / 0.49 / 0.65	-0.51 / -0.42 / **-0.22**	**0.43** / 0.75 / 1.36
	RMSE	1.23 / **1.19** / 1.30	1.53 / 1.40 / **1.39**	**2.14** / 2.48 / 3.4
	R	0.52 / 0.52 / **0.54**	0.21 / 0.41 / **0.45**	**0.69** / 0.66 / 0.66
HNO_3	mean bias	-0.11 / 0.62 / **-0.07**	-0.12 / 0.36 / **-0.10**	
	RMSE	**0.50** / 0.87 / 0.50	**0.50** / 0.91 / 0.65	
	R	0.33 / **0.57** / 0.30	**0.21** / 0.20 / 0.20	
NO_3^-	mean bias	1.78 / **0.11** / 1.51	1.17 / **-0.08** / 0.6	3.19 / **-0.18** / 2.2
	RMSE	2.2 / **0.74** / 1.97	3.55 / **2.71** / 3.02	4.25 / **1.47** / 3.3
	R	0.31 / **0.65** / 0.24	0.19 / **0.32** / 0.21	**0.59** / 0.5 / 0.58
NH_3	mean bias	-0.35 / **-0.11** / -0.33	0.87 / **0.82** / 0.82	
	RMSE	1.77 / **1.72** / 1.76	1.84 / **1.67** / 1.79	
	R	0.44 / **0.46** / 0.44	0.45 / **0.57** / 0.48	
NH_4^+	mean bias	0.66 / **0.19** / 0.69	0.27 / **-0.05** / 0.33	1.16 / **0.63** / 1.42
	RMSE	0.90 / **0.43** / 0.92	0.88 / **0.69** / 0.95	2.03 / **1.4** / 2.5
	R	0.32 / **0.45** / 0.30	0.40 / **0.49** / 0.38	0.43 / **0.45** / 0.41

5.5 Evaluation of surface aerosol pH

In this section and next, we focus on the new diagnostic output proposed in the CY49R1 experiments: aerosol and precipitation pH. The use of EQSAM4Clim has the potential to provide an improved regional representation of aerosol, cloud and precipitation pH, which can act as a potential product provided by CAMS. To date, to our knowledge, such near-real time products

515   on the acidity of aerosol, clouds and precipitations are not available.

Aerosol acidity plays an important role in a variety of aerosol physical and chemical processes as discussed in Freedman et al. (2019) and Pye et al. (2020). In particular, it can influence production rates of secondary inorganic aerosols through heterogeneous reactions and modulate aerosol mass by controlling the gas–particle partitioning of volatile and semi-volatile compounds. Aerosol acidity is usually measured in terms of aerosol pH, which is determined by both aerosol composition and

520   aerosol water (Zhang et al., 2021). Very few direct observations of aerosol pH are available, as it is hard to measure it directly (Li and Jang, 2012). Zhang et al. (2021) propose a data set of aerosol pH computed using ISORROPIA II (Fountoukis and Nenes, 2007) and local meteorological variables in tandem with both gas-phase and aerosol-phase composition observations over the USA and China. In the USA, observational data are available from co-located CASTNET and AMoN sites. In China, hourly

observational data from the data-sharing platform operated by the Comprehensive Observation Network for Air Pollution in Beijing-Tianjin-Hebei and its Surrounding Areas are used. However, the Zhang et al. (2021) data set has only been calculated for the year 2011 for the U.S. and 2017 for China, while the IFS-COMPO data set is for the year 2019, which means that the comparison between the two is only qualitative considering the change in emissions which have occurred over this decade, particularly for the U.S. dataset. We can still use such a comparison to assess the representation of regional variability. We also use the climatological surface pH observations compiled by Pye et al. (2020) and compare the simulated values to recent results from Rosanka et al. (2024).

In Figure 14, we compare the 2019 average of surface aerosol pH simulated by CY49R1 to values simulated for fine mode aerosols only and for 2010 by the AERCHEM and ISORROPIA-II thermodynamical modules implemented in the Messy model as presented in Rosanka et al. (2024), and to climatological observations from Pye et al. (2020). The surface aerosol pH simulated by CY49R1 shows higher values over oceans, ranging from 3 to more than 5 than over continents, where they are comprised between 1.5 and 3.5 in general. This can be explained by two factors : in general, higher relative humidity and thus aerosol water content over oceans, and also, sea-salt aerosols which dominate over oceans are on average more alkaline than other aerosol species. In particular, areas with higher amounts of sea-salt aerosols, such as below 4° S, are the areas with the highest simulated surface pH, with values reaching 5 and above. Over continents, the deserts stand out with lower surface aerosol pH values, because of lower aerosol water. Compared to observations, the CY49R1 simulated values are slightly higher over Europe and China (ranging between 3 and 4 in general) than over US (from 3 and above in the East to closer to 2 in the West). The simulated surface aerosol Ph values are generally too acidic over US, too alkaline over oceans while over central and East Asia the values are more or less in the range of the climatological observations provided by Pye et al. (2020)

The values simulated by CY49R1 match relatively well the ISORROPIA-II simulations from Rosanka et al. (2024) over continents. Over oceans, the values simualted by CY49R1 are significantly higher, which is caused by the fact that diagnostic aerosol water from coarse and super coarse sea-salt is used as an input to the aerosol pH computations : this increases a lot the pH values over oceans, while the aerosol pH computed in Rosanka et al. (2024) is only for fine mode aerosols and this doesn't include aerosol water from coarse sea-salt aerosols. Over continents, the values from ISORROPIA-II and CY49R1 are quite similar, with somewhat higher values for CY49R1, which could be from a different simulated aerosol composition, but also from the fact that diagnostic aerosol water from OM, BC and desert dust are used in CY49R1, which increase somewhat the simulated aerosol pH values. The CY49R1 surface aerosol pH values are much higher than those simulated by AERCHEM : over oceans, this is caused by higher aerosol water with CY49R1 (from the same caused as explained above), and also because the AERCHEM module simulated the acification of sea-salt aerosol (Rosanka et al. (2024)), which is a process not represented in the IFS.

5.6 Evaluation of precipitation pH

In contrast to aerosol pH, precipitation pH is measured routinely by several networks, namely the National Trends Network (NTN) operated by the National Atmospheric Deposition Program (NADP) in the U.S., EMEP in Europe and EANET in East Asia for the regions of interest in this study, made at the same frequency as the measurements of gas-species and particles.

Recently, precipitation pH has also been simulated by the GEOS-CHEM Chemistry Transport Model (CTM) for the year 2013 (Shah et al., 2020), although simulations were conducted at a coarser resolution than the IFS-COMPO simulations presented here and for a different year. In this section, the precipitation pH values simulated by IFS-COMPO are precipitation weighted and compared against the relevant observational data. The simulation of precipitation pH depends on both aerosol composition and precipitation fluxes, and combines uncertainties from both forecasts; this is why we present here yearly and monthly values.

Figure 16 shows the average of the precipitation pH from IFS-COMPO for 2019 for CY49R1. Compared to the aerosol pH values shown in Figure 15, these values are higher (less acidic) reaching values of pH between 4.0-5.0 over oceans and 4.5-5.5 over the majority of the continents. Precipitation pH is more impacted by simulated precipitation fluxes than by aerosol composition, which is why drier areas are generally showing lower pH values, while the opposite is true for wet areas. The comparison of the precipitation pH simulation against observed values over the USA, Europe and South-East Asia reveals that values are generally in the same range of observations, with some exceptions such as e.g. in the Mediterranean. Over the USA, the contrast between Eastern and Western U.S. is more marked in the simulated values than in the observations, although the gradient in pH values across the continent is captured. Over Europe, the simulated values agree well for most of the sites, although the simulated values are too high over Spain (dry and impacted by dust) and the Po Valley (high anthropogenic emissions) indicating some additional challenges for these locations, which includes uncertainties with the simulated precipitation. For East Asia, the simulated values agree favourably for China, while they are more acidic for other countries including Indonesia.

Focusing on the US, comparisons of precipitation pH from CY49R1 against observations are shown in Figure 17. The top two panels show time series of simulated versus observed monthly pH values at two individual sites, namely: South Pass City in Wyoming (42.47°N, 108.8°W) and Clinton in Massachusetts (42.42°N, 71.68°W), i.e., one site at the East Coast and the other at the West Coast, respectively. For South Pass City, the simulated values show a persistent negative bias of 0.2-0.4 (i.e. too acidic); however, the seasonal variability is relatively well captured. The negative bias is probably caused by an overestimate in simulated sulfate, itself perhaps arising from too high SO_2 emissions, as shown by a comparison of surface sulfate simulated by CY49R1 versus CASTNET stations in the regions (not shown). For Clinton, there is a very good agreement between the simulated and observed monthly precipitation pH, with a small negative bias of 0.1-0.2 in the spring. The bottom panel shows a density scatter-plot of a comparison of simulated yearly precipitation pH against corresponding NADP/NTN values over all 248 stations of this network. The agreement is much better than that for aerosol pH, albeit exhibiting a small negative bias of -0.27 pH units. This provides confidence that IFS-COMPO simulates the regional distribution and variability in precipitation pH relatively accurately, which results from a good representation of precipitation fluxes as well as aerosol composition.

Finally, Figure 18 shows a comparison of regional observed and simulated precipitation pH, including data from the GEOS-CHEM CTM as provided by Shah et al. (2020). The GEOS-CHEM CTM data is for the year 2013 instead of 2019, and using a much coarser resolution than IFS-COMPO. For all regions, the simulated values, either by IFS-COMPO or GEOS-CHEM CTM, are too low as compared to observations. The IFS-COMPO average precipitation pH values are in closer agreement with the observed values over the U.S. and Europe, and lower than GEOS-CHEM CTM over Asia.

6 Conclusions

In this study, we have presented a description and an evaluation of the model changes that will form the basis of cycle 49R1 of IFS-COMPO, focusing on the impact of the implementation and use of a simplified thermodynamical equilibrium model, EQSAM4Clim, for the purpose of improving the simulated inorganic gas/particle partitioning and the provision of aerosol/-cloud/precipitation pH simulations. The changes bring a significant improvement in the representation of the nitrogen life cycle, mostly from the use of EQSAM4Clim, which improves the simulated biases for NO_3^- and NH_4^+ over Europe, South-East Asia and the U.S. . This significantly improves on the simulated PM2.5 and, to a lesser extent, AOD. This provides confidence that for the future, the CAMS system will have an improved capability of simulating more accurate surface aerosol composition which is one of the important products of the service.

In addition, we have shown that the representation of aerosol and precipitation acidity in IFS-COMPO is captured with sufficient accuracy as to envisage their inclusion in the CAMS product portfolio. A preliminary evaluation of some of these potential products have been presented here, with a reasonable agreement of simulated precipitation pH against routine observations in Europe, Asia and U.S.. More evaluation is needed to fully assess the new pH diagnostics, especially concerning seasonal variability at specific locations, where this study acts as the groundwork for future datasets that could be provided by CAMS.

The other updates included in cycle 49R1 generally result in a positive impact on skill scores when applied in tandem with EQSAM4Clim. In particular, the biases in the AOD and Ångström Exponent are decreased over almost all global regions as compared to cycle 48R1. However, there are instances of an increased positive bias for e.g. AOD at 500nm and PM2.5 in spring/summertime over U.S. and China, and a persistent low bias in PM10 which require some attention. Some of the PM2.5 summertime biases are caused by too high secondary organic aerosol of biogenic origin, which currently depend on static emissions of isoprene and monoterpenes from CAMS_GLOB_BIO. A better representation of the variability of these emissions depending on the meteorological and vegetation condition could probably help in this respect, and is one direction explored for the further improvement of global CAMS products. IFS-COMPO also clearly does not capture some sources or processes that lead to the formation of coarser particles as indicated by the systematic low bias in PM10. More work is needed for a better representation of PM10 in IFS-COMPO.

References

Agusti-Panareda, A., Diamantakis, M., Bayona, V., Klappenbach, F., and Butz, A.: Improving the inter-hemispheric gradient of total column atmospheric CO_2 and CH_4 in simulations with the ECMWF semi-Lagrangian atmospheric global model, Geoscientific Model Development, 10, 1–18, 2017.

Albert, M. F. M. A., Anguelova, M. D., Manders, A. M. M., Schaap, M., and de Leeuw, G.: Parameterization of oceanic whitecap fraction based on satellite observations, Atmos. Chem. Phys., 16, 13 725–13 751, 2016.

Angle, K., Neal, E., and Grassian, V.: Enhanced Rates of Transition-Metal-Ion-Catalyzed Oxidation of S(IV) in Aqueous Aerosols: Insights into Sulfate Aerosol Formation in the Atmosphere, Environ. Sci. Technol., 55, 10 291–10 299, 2021.

Anguelova, M. D. and Webster, F.: Whitecap coverage from satellite measurements: A first step toward modeling the variability of oceanic whitecaps, J. Geophys. Res, 111, C03 017, 2006.

Ault, A. P.: Aerosol Acidity: Novel Measurements and Implications for Atmospheric Chemistry, Acc. Chem. Res., 53, 1703–1714, 2020.

Bellouin, N., Rae, J., Jones, A., Johnson, C., Haywood, J., and Boucher, O.: Aerosol forcing in the Climate Model Intercomparison Project (CMIP5) simulations by HadGEM2-ES and the role of ammonium nitrate, J. Geophys. Res., 116, D20 206, 2011.

Boucher, O., Pham, M., and Venkataraman, C.: Simulation of the atmospheric sulfur cycle in the Laboratoire de Meteorologie Dynamique general circulation model: Model description, model evaluation, and global and European budgets, Note Scientifique de l'IPSL, 23, 27 pp., 2002.

Cao, H., Henze, D. K., Zhu, L., Shephard, M. W., Cady-Pereira, K., Dammers, E., Sitwell, M., Heath, N., Lonsdale, C., Bash, J. O., Miyazaki, K., Flechard, C., Fauvel, Y., Kruit, R. W., Feigenspan, S., Brümmer, C., Schrader, F., Twigg, M. M., Leeson, S., Tang, Y. S., Stephens, A. C. M., Braban, C., Vincent, K., Meier, M., Seitler, E., Geels, C., Ellermann, T., Sanocka, A., and Capps, S. L.: 4D-Var Inversion of European NH3 Emissions Using CrIS NH3 Measurements and GEOS-Chem Adjoint With Bi-Directional and Uni-Directional Flux Schemes, Journal of Geophysical Research: Atmospheres, 127, e2021JD035 687, https://doi.org/https://doi.org/10.1029/2021JD035687, e2021JD035687 2021JD035687, 2022.

Chen, L., Peng, C., Gu, W., Fu, H., Jian, X., Zhang, H., Zhang, G., Zhu, J., Wang, X., and Tang, M.: On mineral dust aerosol hygroscopicity, Atmos. Chem. Phys., 20, 13 611–13 626, https://doi.org/10.5194/acp-20-13611-2020, 2020.

Chin, M., Jacob, D. J., Gardner, G. M., Foreman-Fowler, M. S., Spiro, P. A., and Savoie, D. L.: A global three-dimensional model of tropospheric sulfate, J. Geophys. Res., 101, D06 304, https://doi.org/10.1029/96JD01221, 1996.

Croft, B., Lohmann, U., Martin, R. V., Stier, P., Wurzler, S., Feichter, J., Posselt, R., and Ferrachat, S.: Aerosol size-dependent below-cloud scavenging by rain and snow in the ECHAM5-HAM, Atmos. Chem. Phys., 9, 4653–4675, 2009.

de Bruine, M., Krol, M., van Noije, T., Le Sager, P., and Röckmann, T.: The impact of precipitation evaporation on the atmospheric aerosol distribution in EC-Earth v3.2.0, Geosci. Model Dev., 11, 1443–1465, 2018.

Diamantakis, M. and Flemming, J.: Global mass fixer algorithms for conservative tracer transport in the ECMWF model, Geoscientific Model Development, 7, 965–979, 2014.

ECMWF: IFS Documentation CY48R1 - Part VIII Atmospheric composition, 8, ECMWF, https://doi.org/10.21957/749dc09059, 2023.

Flemming, J., Huijnen, V., Arteta, J., Bechtold, P., Beljaars, A., Blechschmidt, A.-M., Diamantakis, M., Engelen, R. J., Gaudel, A., Inness, A., Jones, L., Josse, B., Katragkou, E., Marecal, V., Peuch, V.-H., Richter, A., Schultz, M. G., Stein, O., and Tsikerdekis, A.: Tropospheric chemistry in the Integrated Forecasting System of ECMWF, Geosci. Model Dev., 8, 975–1003, 2015.

Flemming, J., Benedetti, A., Inness, A., Engelen, R. J., Jones, L., Huijnen, V., Remy, S., Parrington, M., Suttie, M., Bozzo, A., et al.: The CAMS interim Reanalysis of Carbon Monoxide, Ozone and Aerosol for 2003–2015, Atmospheric Chemistry and Physics, 17, 1945–1983, 2017.

Fountoukis, C. and Nenes, A.: ISORROPIA II: a computationally efficient thermodynamic equilibrium model for K+–Ca2+–Mg2+–NH4+–Na+–SO–NO–Cl--H2O aerosols, Atmospheric Chemistry and Physics, 7, 4639–4659, https://doi.org/10.5194/acp-7-4639-2007, 2007.

Freedman, M., Ott, E.-J. E., and Marak, K.: Role of pH in Aerosol Processes and Measurement Challenges, J. Phys. Chem. A, 123, 1275–1284, 2019.

Gasteiger, J. and Wiegner, M.: MOPSMAP v1.0: a versatile tool for the modeling of aerosol optical properties, Geosci. Model Dev., 11, 2739–2762, https://doi.org/10.5194/gmd-11-2739-2018, 2018.

Gong, S.: A parameterization of sea-salt aerosol source function for sub- and super-micron particles, Global Biogeochem. Cycles, 17, 1097, 2003.

Hauglustaine, D. A., Balkanski, Y., and Schulz, M.: A global model simulation of present and future nitrate aerosols and their direct radiative forcing of climate, Atmos. Chem. Phys., 14, 11 031–11 064, 2014.

Holben, B. N., Eck, T., Slutsker, I., Tanre, D., Buis, J., Setzer, A., Vermote, E., Reagan, J., Kaufman, Y., Nakajima, T., et al.: AERONETâA federated instrument network and data archive for aerosol characterization, Remote sensing of environment, 66, 1–16, 1998.

Hortal, M.: The development and testing of a new two-time-level semi-Lagrangian scheme (SETTLS) in the ECMWF forecast model, Quarterly Journal of the Royal Meteorological Society, 128, 1671–1687, 2002.

Huijnen, V., Flemming, J., Chabrillat, S., Errera, Q., Christophe, Y., Blechschmidt, A.-M., Richter, A., and Eskes, H.: C-IFS-CB05-BASCOE: stratospheric chemistry in the Integrated Forecasting System of ECMWF, Geoscientific Model Development, 9, 3071–3091, 2016.

Huijnen, V., Pozzer, A., Arteta, J., Brasseur, G., Bouarar, I., Chabrillat, S., Christophe, Y., Doumbia, T., Flemming, J., Guth, J., Josse, B., Karydis, V. A., Marécal, V., and Pelletier, S.: Quantifying uncertainties due to chemistry modelling â evaluation of tropospheric composition simulations in the CAMS model (cycle 43R1), Geosci. Model Dev., 12, 1725–1752, 2019.

Huijnen, V., Le Sager, P., Köhler, M. O., Carver, G., Rémy, S., Flemming, J., Chabrillat, S., Errera, Q., and van Noije, T.: OpenIFS/AC: atmospheric chemistry and aerosol in OpenIFS 43r3, Geosci. Model Dev., 15, 6221–6241, https://doi.org/10.5194/gmd-15-6221-2022, 2022.

Inness, A., Baier, F., Benedetti, A., Bouarar, I., Chabrillat, S., Clark, H., Clerbaux, C., Coheur, P., Engelen, R. J., Errera, Q., Flemming, J., George, M., Granier, C., Hadji-Lazaro, J., Huijnen, V. andHurtmans, D., Jones, L., Kaiser, J. W., Kapsomenakis, J., Lefever, K., Leitâo, J., Razinger, M., Richter, A., Schultz, M. G., Simmons, A. J., Suttie, M., Stein, O., Thépaut, J.-N., Thouret, V., Vrekoussis, M., and the MACC team: The MACC reanalysis: an 8 yr data set of atmospheric composition, Atmospheric Chemistry and Physics, 13, 4073–4109, 2013.

Inness, A., Ades, M., Agustí-Panareda, A., Barré, J., Benedictow, A., Blechschmidt, A.-M., Dominguez, J. J., Engelen, R., Eskes, H., Flemming, J., Huijnen, V., Jones, L., Kipling, Z., Massart, S., Parrington, M., Peuch, V.-H., Razinger, M., Remy, S., Schulz, M., , and Suttie, M.: The CAMS reanalysis of atmospheric composition, Atmospheric Chemistry and Physics, 19, 3515–3556, 2019.

Journet, E., Balkanski, Y., and Harrison, S. P.: A new data set of soil mineralogy for dust-cycle modeling, Atmos. Chem. Phys., 14, 3801–3816, 2014.

Kaiser, J., Heil, A., Andreae, M., Benedetti, A., Chubarova, N., Jones, L., Morcrette, J.-J., Razinger, M., Schultz, M., Suttie, M., et al.: Biomass burning emissions estimated with a global fire assimilation system based on observed fire radiative power, Biogeosciences, 9, 527, 2012.

Kandler, K., Schutz, L., Deutscher, C., Ebert, M., Hofmann, H., Jackel, S., Jaenicke, R., Knippertz, P., Lieke, K., Massling, A., Petzold, A., Schladitz, A., Weinzierl, B., Wiedenshohler, A., Zorn, S., and Weinbruch, S.: Size distribution, mass concentration, chemical and mineralogical composition and derived optical parameters of the boundary layer aerosol at Tinfou, Morocco, during SAMUM 2006, Tellus B, 61, 32–50, https://doi.org/10.1111/j.1600-0889.2008.00385.x, 2009.

Karydis, V. A., Tsimpidi, A. P., Pozzer, A., and Lelieveld, J.: How alkaline compounds control atmospheric aerosol particle acidity, Atmos. Chem. Phys., 21, 14 983–15 001, https://doi.org/10.5194/acp-21-14983-2021, 2021.

Köhler, H.: The nucleus in and the growth of hygroscopic droplets, Trans. Faraday Soc., 32, 1152–1161, 1936.

Lee, C., Martin, R. V., van Donkelaar, A., Lee, H., Dickerson, R. R., Hains, J. C., Krotkov, N., Richter, A., Vinnikovand, K., and Schwab, J. J.: S02 emissions and lifetimes: Estimates from inverse modeling using in situ and global, space-based (SCIAMACHY and OMI) observations, J. Geophys. Res., 116, D06 304, https://doi.org/10.1029/2010JD014758, 2011.

Li, J. and Jang, M.: Aerosol Acidity Measurement Using Colorimetry Coupled With a Reflectance UV-Visible Spectrometer, Aerosol Sci. Technol., 46, 833–842, https://doi.org/10.1080/02786826.2012.669873, 2012.

Luo, G., Yu, F., and Schwab, J.: Revised treatment of wet scavenging processes dramatically improves GEOS-Chem 12.0.0 simulations of surface nitric acid, nitrate, and ammonium over the United States, Geosci. Model Dev., 12, 3439–3447, 2019.

Luo, Z., Zhang, Y., Chen, W., Van Damme, M., Coheur, P.-F., and Clarisse, L.: Estimating global ammonia (NH3) emissions based on IASI observations from 2008 to 2018, Atmos. Chem. Phys., 22, 10 375–10 388, 2022.

Metzger, S., Dentener, F., Pandis, S., and Lelieveld, J.: Gas/aerosol partitioning: 1. A computationally efficient model, J. Geophys. Res., 107, 4312, 2002.

Metzger, S., Steil, B., Xu, L., Penner, J. E., and Lelieveld, J.: New representation of water activity based on a single solute specific constant to parameterize the hygroscopic growth of aerosols in atmospheric models, Atmos. Chem. Phys., 12, 5429–5446, https://doi.org/10.5194/aacp-12-5429-2012, 2012.

Metzger, S., Steil, B., Abdelkader, M., Klingmüller, K., Xu, L., Penner, J. E., Fountoukis, C., Nenes, A., and Lelieveld, J.: Aerosol water parameterisation: a single parameter framework, Atmos. Chem. Phys., 16, 7213–7237, 2016.

Metzger, S., Abdelkader, M., Steil, B., and Klingmueller, K.: Aerosol water parameterization: long-term evaluation and importance for climate studies, Atmos. Chem. Phys., 18, 16 747–16 774, https://doi.org/10.5194/acp-18-16747-2018, 2018.

Metzger, S., Rémy, S., Williams, J. E., Huijnen, V., and Flemming, J.: A revised parameterization for aerosol, cloud and precipitation pH for use in chemical forecasting systems (EQSAM4Clim-v12), Geosci. Model Dev., [preprint], https://doi.org/10.5194/egusphere-2023-2930, 2023.

Michou, M., Nabat, P., and Saint-Martin, D.: Development and basic evaluation of a prognostic aerosol scheme (v1) in the CNRM Climate Model CNRM-CM6, Geoscientific Model Development, 8, 501–531, 2015.

Monahan, E. C., Spiel, D. E., and Davidson, K. L.: A model of marine aerosol generation via whitecaps and wave disruption, in: Oceanic Whitecaps and Their Role in AirâSea Exchange Processes, edited by Monahan, E. C. and MacNiocaill, G., pp. 167–174, D. Reidel, 1986.

Myriokefalitakis, S., Bergas-Massó, E., Gonçalves-Ageitos, M., Pérez García-Pando, C., van Noije, T., Le Sager, P., Ito, A., Athanasopoulou, E., Nenes, A., Kanakidou, M., Krol, M. C., and Gerasopoulos, E.: Multiphase processes in the EC-Earth model and their relevance to the atmospheric oxalate, sulfate, and iron cycles, Geosci. Model Dev., 15, 3079–3120, https://doi.org/10.5194/gmd-15-3079-2022, 2022.

Nault, B. A., Campuzano-Jost, P., Day, D. A., Jo, D. S., Schroder, J. C., Allen, H. M., Bahreini, R., Bian, H., Blake, D. R., Chin, M., Clegg, S. L., Colarco, P. R., Crounse, J. D., Cubison, M. J., DeCarlo, P. F., Dibb, J. E., Diskin, G. S., Hodzic, A., Hu, W., Katich, J. M., Kim, M. J., Kodros, J. K., Kupc, A., Lopez-Hilfiker, F. D., Marais, E. A., Middlebrook, A. M., Andrew Neuman, J., Nowak, J. B., Palm, B. B.,

750   Paulot, F., Pierce, J. R., Schill, G. P., Scheuer, E., Thornton, J. A., Tsigaridis, K., Wennberg, P. O., Williamson, C. J., and Jimenez, J. L.: Chemical transport models often underestimate inorganic aerosol acidity in remote regions of the atmosphere., Commun Earth Environ, 2, 93, 2021.

O'Dowd, C., Smith, M., Consterdine, I., and Lowe, J.: Marine aerosol, sea-salt, and the marine sulphur cycle: a short review, Atmospheric Environment, 31, 73–80, 1997.

755   Peuch, V.-H., Engelen, R., Rixen, M., Dee, D., Flemming, J., Suttie, M., Ades, M., Agusti-Panareda, A., Ananasso, C., Andersson, E., Armstrong, D., Barre, J., Bousserez, N., Dominguez, J. J., Garrigues, S., Inness, A., Jones, L., Kipling, Z., Letertre-Danczak, J., Parrington, M., Razinger, M., Ribas, R., Vermoote, S., Yang, X., Simmons, A., de Marcilla, J. G., and Thepaut, J.-N.: The Copernicus Atmosphere Monitoring Service: From Research to Operations, Bulletin of the American Meteorological Society, 103, E2650 – E2668, https://doi.org/https://doi.org/10.1175/BAMS-D-21-0314.1, 2022.

760   Pye, H. O. T., Nenes, A., Alexander, B., Ault, A. P., Barth, M. C., Clegg, S. L., Collett Jr., J. L., Fahey, K. M., Hennigan, C. J., Herrmann, H., Kanakidou, M., Kelly, J. T., Ku, I.-T., McNeill, V. F., Riemer, N., Schaefer, T., Shi, G., T., A., Walker, J. T., Wang, T., Weber, R., Xing, J., Zaveri, R. A., and Zuend, A.: The acidity of atmospheric particles and clouds, Atmos. Chem. Phys., 20, 4809–4888, https://doi.org/10.5194/acp-20-4809-2020, 2020.

Qu, Z., Henze, D. K., Li, C., Theys, N., Wang, Y., Wang, J., Han, J., Shim, C., Dickerson, R. R., and Ren, X.: SO2 Emission Estimates Using

765   OMI SO2 Retrievals for 2005–2017, J. Geophys. Res., 124, 18 667–18 690, https://doi.org/10.1029/2019JD030243, 2019.

Reay, D., Dentener, F., Smith, P., Grace, J., and Feely, R.: Global nitrogen deposition and carbon sinks, Nature Geosci, pp. 430–437, https://doi.org/10.1038/ngeo230, 2008.

Reddy, M. S., Boucher, O., Bellouin, N., Schulz, M., Balkanski, Y., Dufresne, J.-L., and Pham, M.: Estimates of global multicomponent aerosol optical depth and direct radiative perturbation in the Laboratoire de Météorologie Dynamique general circulation model, J. Geo-

770   phys. Res., 110, D10S16, 2005.

Remy, S. and Anguelova, M.: Improving the Representation of Whitecap Fraction and Sea Salt Aerosol Emissions in the ECMWF IFS-AER, Remote Sens., 13, 4856, https://doi.org/10.3390/rs13234856, 2021.

Rémy, S., Kipling, Z., Flemming, J., Boucher, O., Nabat, P., Michou, M., Bozzo, A., Ades, M., Huijnen, V., Benedetti, A., Engelen, R., Peuch, V.-H., and Morcrette, J.-J.: Description and evaluation of the tropospheric aerosol scheme in the European Centre for Medium-Range

775   Weather Forecasts (ECMWF) Integrated Forecasting System (IFS-AER, cycle 45R1), Geoscientific Model Development, 12, 4627–4659, https://doi.org/10.5194/gmd-12-4627-2019, 2019.

Rémy, S., Kipling, Z., Huijnen, V., Flemming, J., Nabat, P., Michou, M., Ades, M., Engelen, R., and Peuch, V.-H.: Description and evaluation of the tropospheric aerosol scheme in the Integrated Forecasting System (IFS-AER, cycle 47R1) of ECMWF, Geoscientific Model Development, 15, 4881–4912, https://doi.org/10.5194/gmd-15-4881-2022, 2022.

780   Rosanka, S., Tost, H., Sander, R., Jöckel, P., Kerkweg, A., and Taraborrelli, D.: How non-equilibrium aerosol chemistry impacts particle acidity: the GMXe AERosol CHEMistry (GMXe–AERCHEM, v1.0) sub-submodel of MESSy, Geosci. Model Dev., 17, 2597–2615, 2024.

Seinfeld, J. and Pandis, S.: Atmospheric Chemistry and Physics: From Air Pollution to Climate Change - second edition, New Jersey: John Wiley and Sons, 2006.

785   Shah, V., Jacob, D. J., Moch, J. M., Wang, X., and Zhai, S.: Global modeling of cloud water acidity, precipitation acidity, and acid inputs to ecosystems, Atmos. Chem. Phys., 20, 12 223–12 245, https://doi.org/10.5194/acp-20-12223-2020, 2020.

Sogacheva, L., Popp, T., Sayer, A. M., Dubovik, O., Garay, M. J., Heckel, A., Hsu, N. C., Jethva, H., Kahn, R. A., Kolmonen, P., Kosmale, M., de Leeuw, G., Levy, R. C., Litvinov, P., Lyapustin, A., North, P., Torres, O., and Arola, A.: Merging regional and global aerosol optical depth records from major available satellite products, Atmos. Chem. Phys., 20, 2031–2056, 2020.

790   Soulie, A., Granier, C., Darras, S., Zilbermann, N., Doumbia, T., Guevara, M., Jalkanen, J.-P., Keita, S., Liousse, C., Crippa, M., Guizzardi, D., Hoesly, R., and Smith, S.: Global Anthropogenic Emissions (CAMS-GLOB-ANT) for the Copernicus Atmosphere Monitoring Service Simulations of Air Quality Forecasts and Reanalyses, Earth Syst. Sci. Data Discuss. [preprint], https://doi.org/10.5194/essd-2023-306, 2023.

Sun, Y., Guo, J., Li, Y., Luo, G., Li, L., Yuan, H., Mur, L. A. J., and Guo, S.: Negative effects of the simu-
795   lated nitrogen deposition on plant phenolic metabolism: A meta-analysis, Science of The Total Environment, 719, 137 442, https://doi.org/https://doi.org/10.1016/j.scitotenv.2020.137442, 2020.

Tilgner, A., Schaefer, T., Alexander, B., Barth, M., Collett Jr., J., Fahey, K., Nenes, A., Pye, H., Herrmann, H., and McNeill, V.: Acidity and the multiphase chemistry of atmospheric aqueous particles and clouds, Atmospheric Chemistry and Physics, 21, 13 483–13 536, https://doi.org/10.5194/acp-21-13483-2017, 2021.

800   Van Damme, M., Clarisse, L., Whitburn, S., Hadji-Lazero, J., Hurtmans, D., Clerbaux, C., and Coheur, P.-F.: Industrial and agricultural ammonia point sources exposed, Nature, 564, 99–103, https://doi.org/10.1038/s41586-018-0747-1, 2018.

van Noije, T. P. C., Le Sager, P., Segers, A. J., v. V. P. F. J., Krol, M. C., Hazeleger, W., Williams, J., and Chambers, S. D.: Sim-ulation of tropospheric chemistry and aerosols with the climate model EC-Earth, Geoscientific Model Development, 7, 2435–2475, https://doi.org/10.5194/gmd-7-2435-2014, 2014.

805   Verheggen, B., Cozic, J., Weingartner, E., Bower, K., Mertes, S., Connolly, P., Gallagher, M., Flynn, M., Choularton, T., and Baltensperger, U.: Aerosol partitioning between the interstitial and the condensed phase in mixed-phase clouds, Journal of Geophysical Research: Atmo-spheres, 112, https://doi.org/https://doi.org/10.1029/2007JD008714, 2007.

Wang, R., Goll, D., Balkanski, Y., Hauglustaine, D., Boucher, O., Ciais, P., Janssens, I., Penuelas, J., Guenet, B., Sardans, J., Bopp, L., Vuichard, N., Zhou, F., Li, B., Piao, S., Peng, S., Huang, Y., and Tao, S.: Global forest carbon uptake due to nitrogen and phosphorus
810   deposition from 1850 to 2100., Glob Change Biol., 23, 4854–4872, 2017.

Williams, J. E., Strunk, A., Huijnen, V., and van Weele, M.: The application of the Modified Band Approach for the calculation of on-line photodissociation rate constants in TM5: implications for oxidative capacity, Geoscientific Model Development, 5, 15–35, https://doi.org/10.5194/gmd-5-15-2012, 2012.

Williams, J. E., van Velthoven, P., and Brenninkmeijer, C.: Quantifying the uncertainty in simulating global tropospheric composition due
815   to the variability in global emission estimates of Biogenic Volatile Organic Compounds, Atmospheric Chemistry and Physics, 13, 2857–2891, https://doi.org/10.5194/acp-13-2857-2013, 2013.

Williams, J. E., Huijnen, V., Bouarar, I., Meziane, M., Schreurs, T., Pelletier, S., Marecal, V., Josse, B., and Flemming, J.: Regional evalu-ation of the performance of the global CAMS chemical modeling system over the United States (IFS cycle 47r1), Geoscientific Model Development, 15, 4657–4687, https://doi.org/10.5194/gmd-15-4657-2022, 2022.

820   Wiscombe, W. J.: Improved Mie scattering algorithms, Applied Optics, 19, 1505–1509, 1980.

Yarwood, G., Rao, S., Yocke, M., and Whitten, G.: Updates to the carbon bond chemical mechanism: CB05, Final report to the US EPA, EPA Report Number: RT-0400675, available at: http://www.camx.com (last access 03 April 2019), 2005.

Zhang, B., Shen, H., Liu, P., Guo, H., Hu, Y., Chen, Y., Xie, S., Xi, Z., Skipper, T. N., and Russell, A. G.: Significant contrasts in aerosol acidity between China and the United States, Atmos. Chem. Phys., 21, 8341–8356, https://doi.org/10.5194/acp-21-8341-2021, 2021.
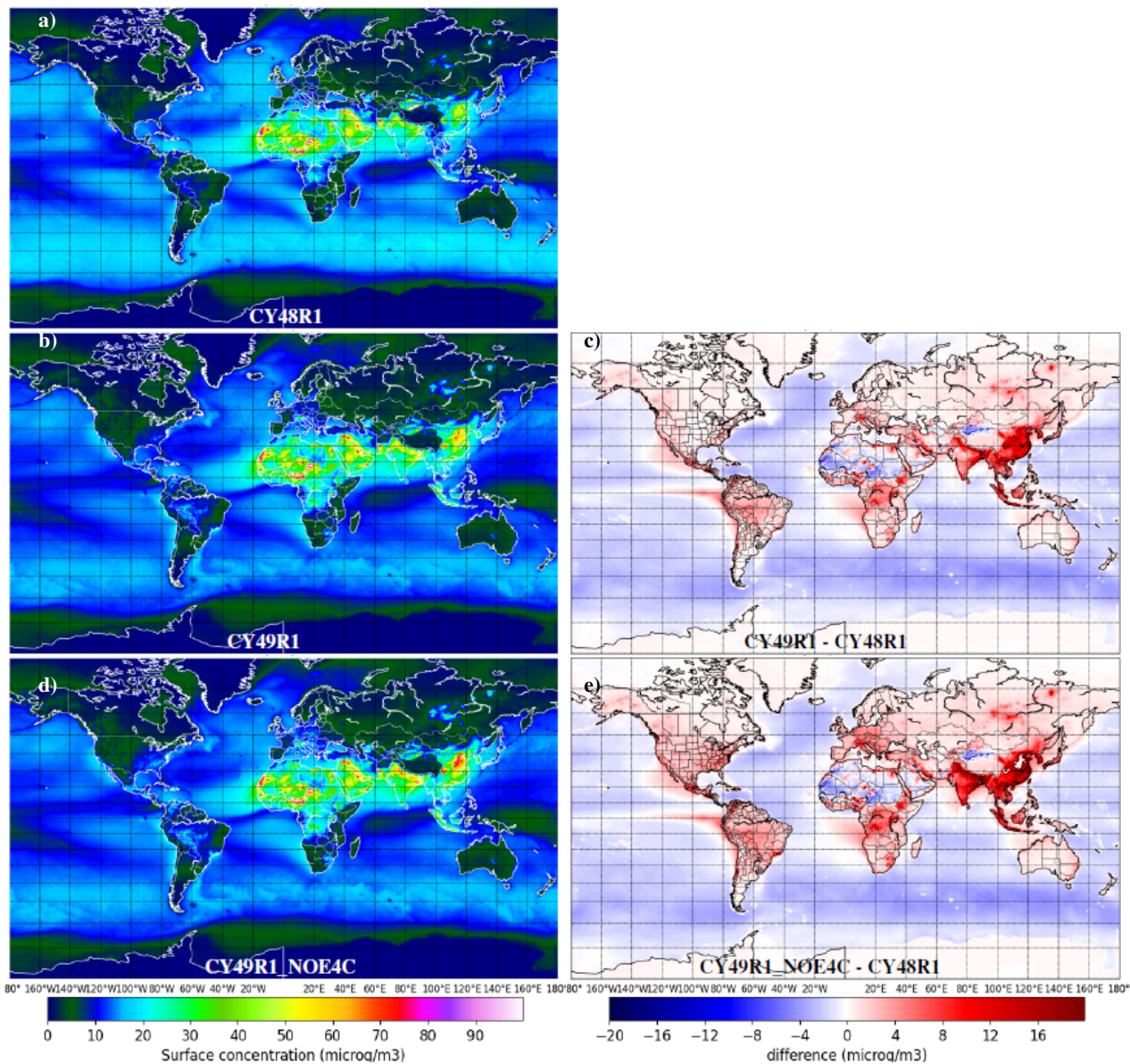
Figure 5. Global mean PM2.5 distributions in μg/m³ (left, panels a, b, d) as simulated in CY48R1, CY49R1 and CY49R1_NOE4C when ran in cycling forecast mode during 2019. The right column (panels c and e) shows the absolute difference in PM 2.5 distributions as compared against the CY48R1 values. Units are in $\mu g/m^3$.
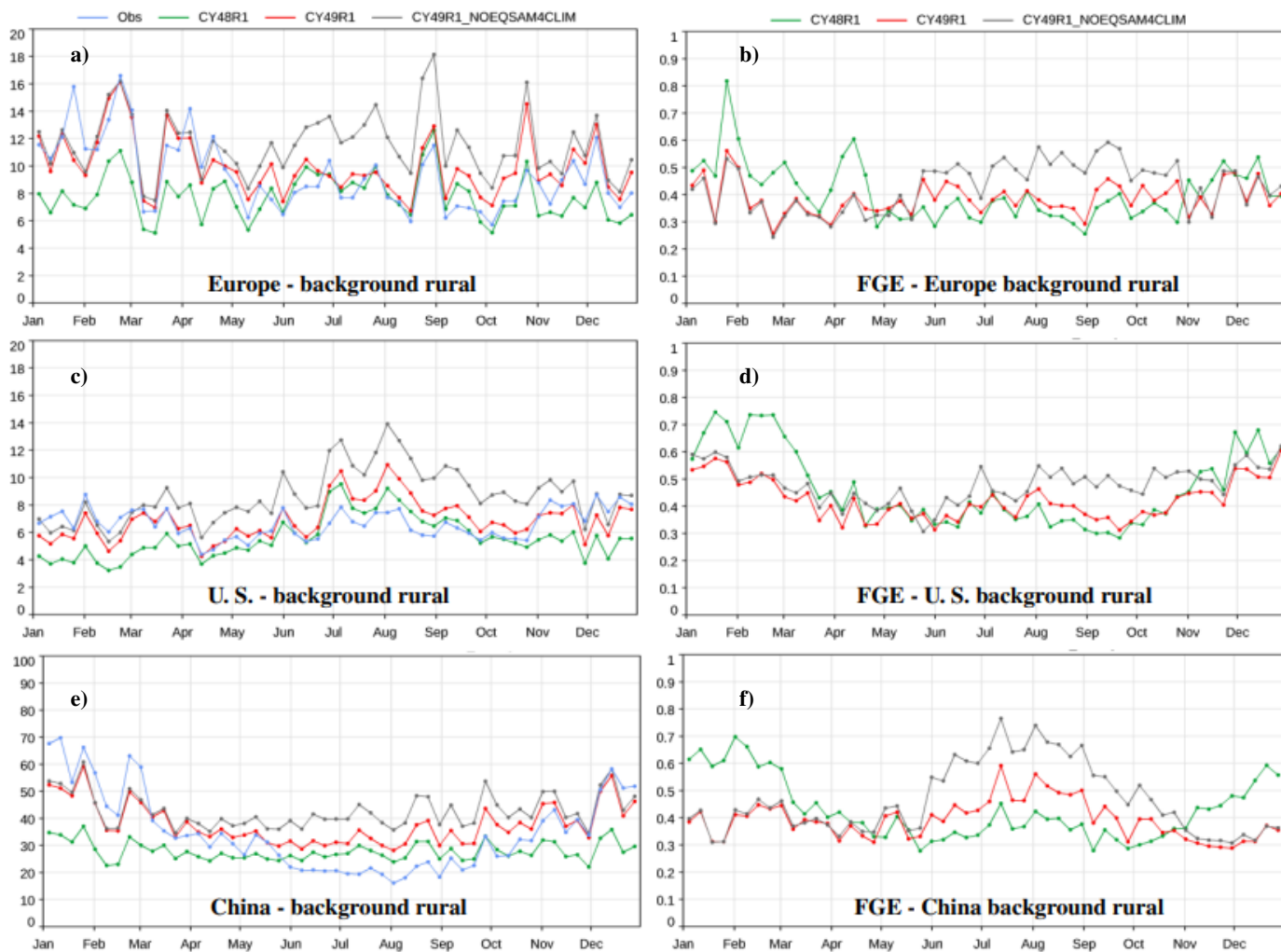
Figure 6. Comparison of observed and simulated weekly PM2.5 concentrations for 2019 over background rural stations in Europe, U.S. and China is shown in the left column (panels a, c, e). The corresponding Fractional Gross Error (FGE) of simulated PM2.5 against observations is shown in the right column (panels b, d, f). Units are in $\mu g/m^3$.
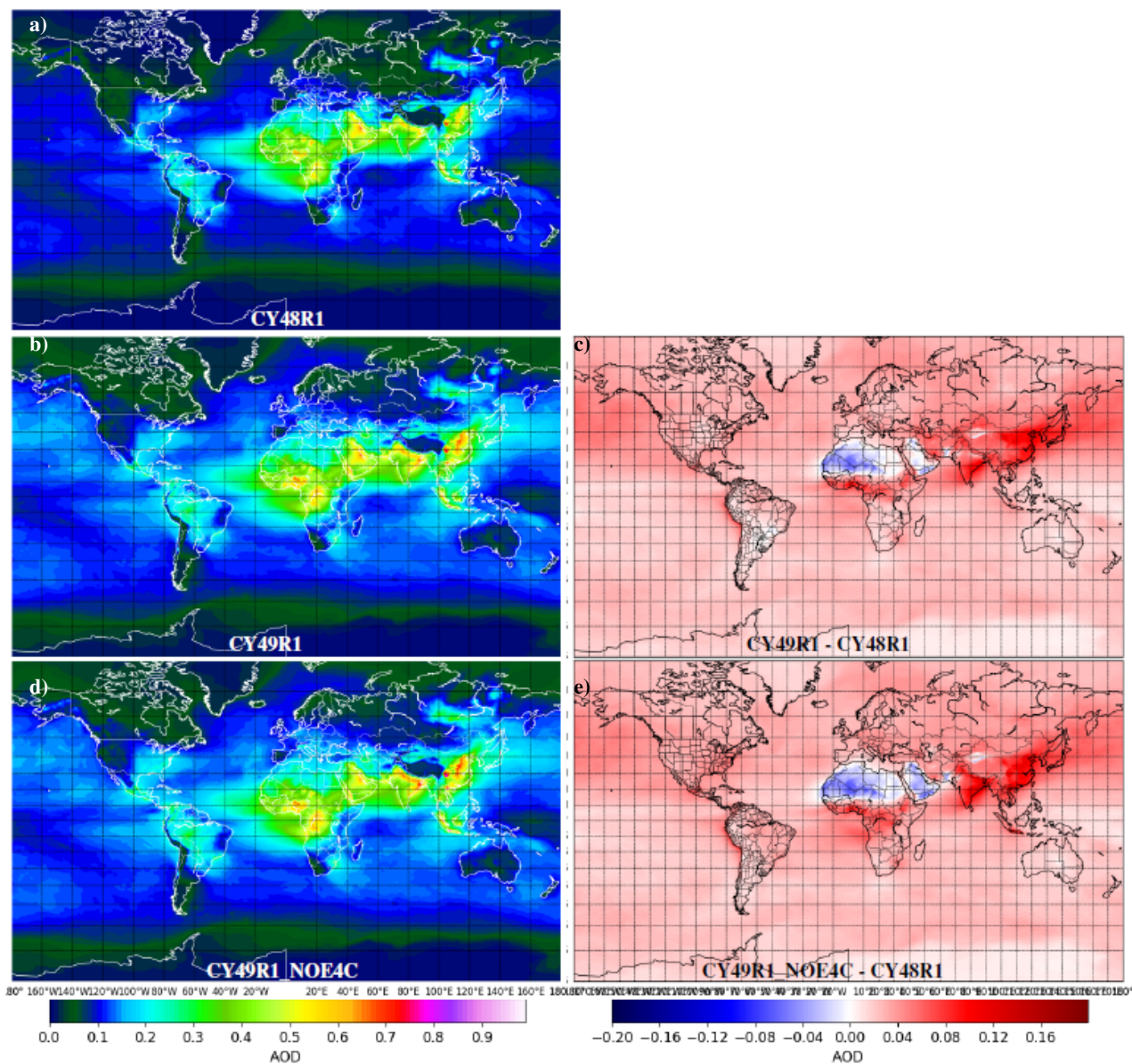
Figure 7. 2019 global mean AOD at 550nm (panels a, b, d, left) as simulated by the CY48R1, CY49R1 and CY49R1_NOE4C experiments. Right (panels c,f), difference with CY48R1 values. The 2019 average of VIIRS AOD at 550nm is also shown top right.
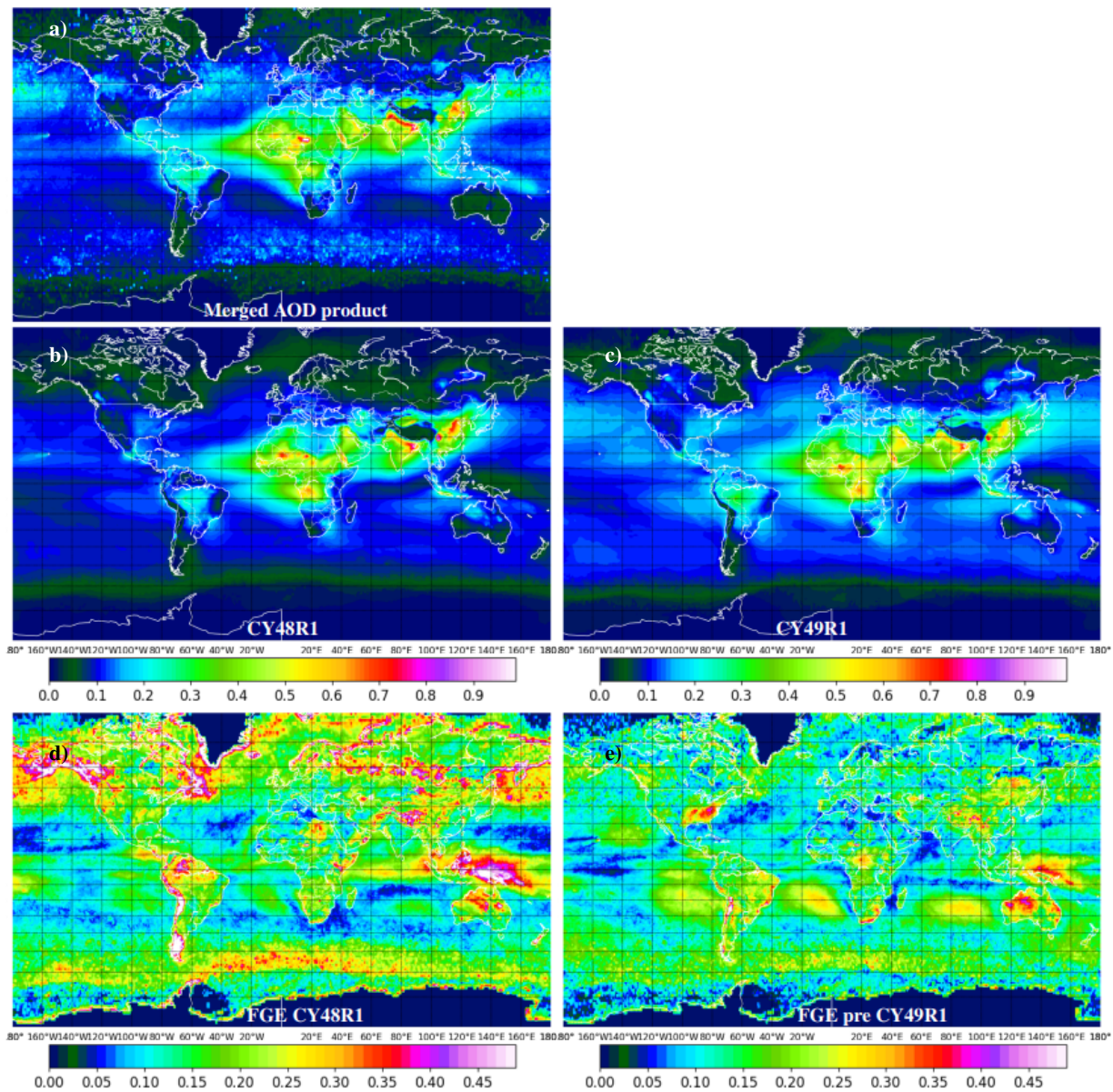
Figure 8. Panel a (top), 2017 average of the merged AOD at 550nm product. Panels b and c, 2017 average of CY48R1 (left) and CY49R1 (right) simulated AOD at 550nm. Panels d and e, 2017 average of Fractional Gross Error (FGE) of monthly simulated vs observed AOD at 550nm for CY48R1 (left) and CY49R1 (right).
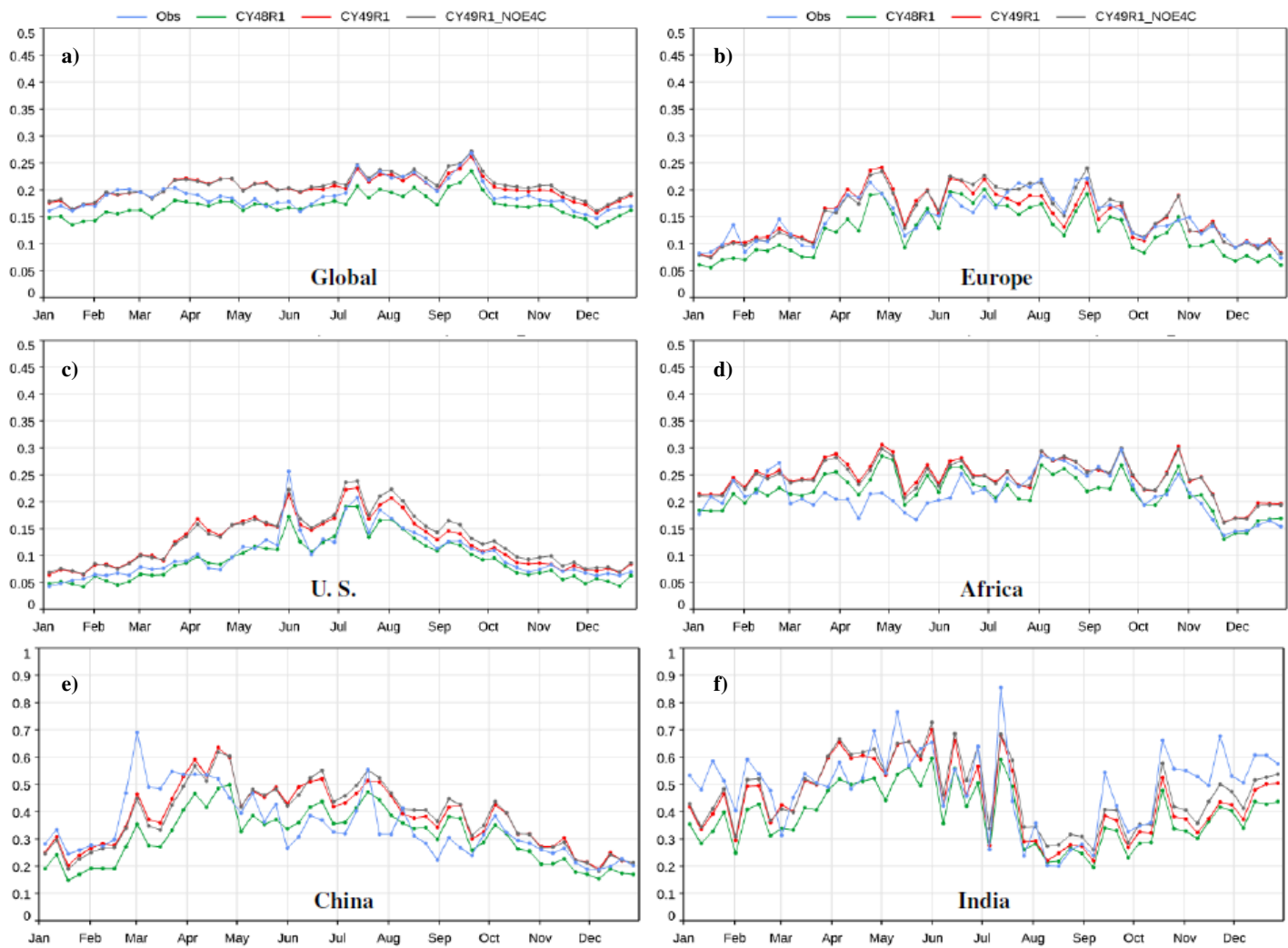
Figure 9. A comparison of the global (panel a, top left) and regional (other panels) weekly simulated and observed AOD (AERONET level 2) at 500nm for 2019. The comparison is made on 461 AERONET sites globally, 113 sites in Europe, 119 sites over the U.S., 68 sites in Africa, 23 in China and 16 in India.
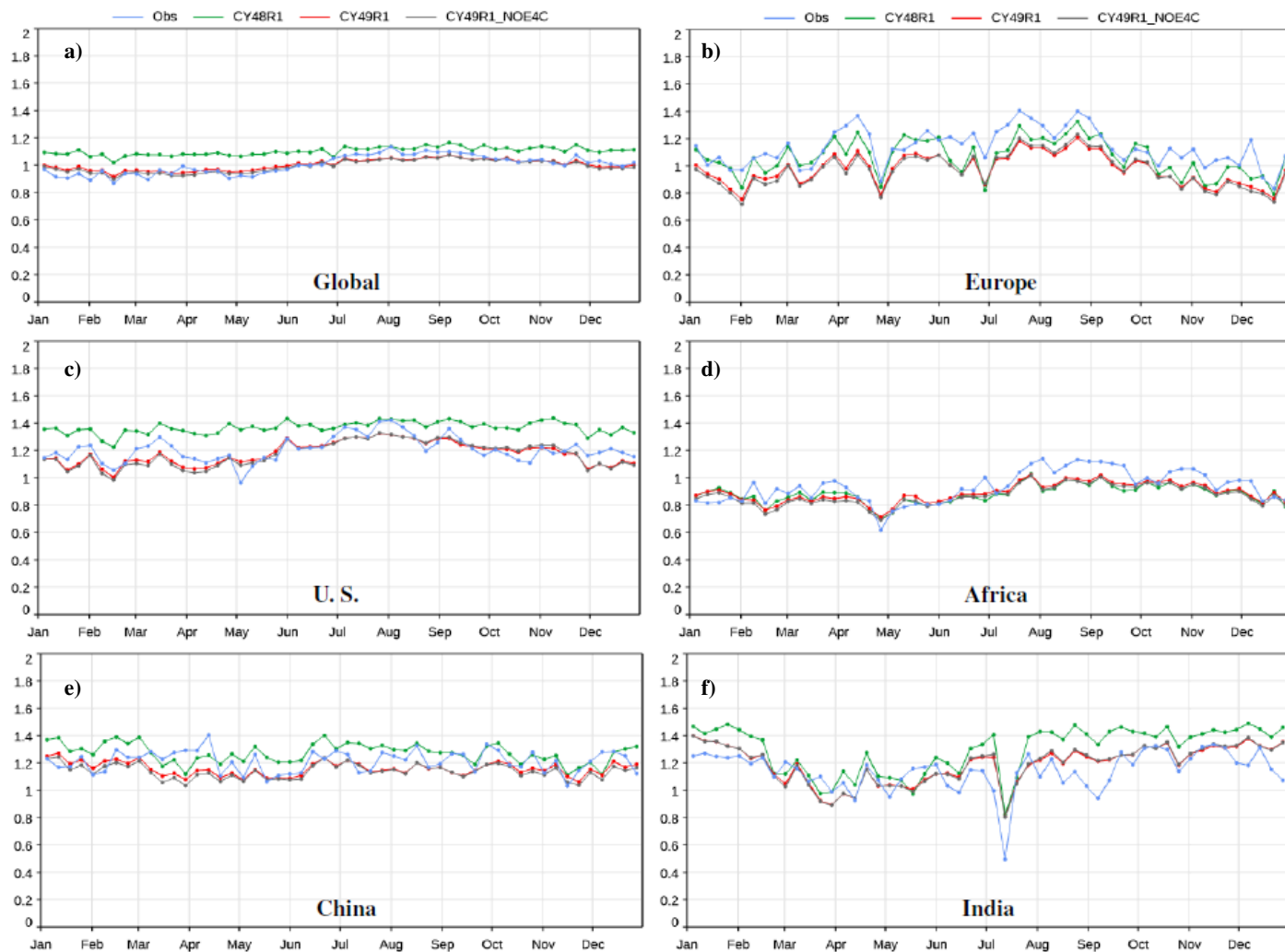
Figure 10. A comparison of the simulated and observed weekly global (panel a, top left) and regional (other panels) Ångström exponent (440-865nm) for 2019. The comparison is made on 472 AERONET sites globally, 118 sites in Europe, 119 sites over the U.S., 68 sites in Africa, 23 in China and 17 in India.
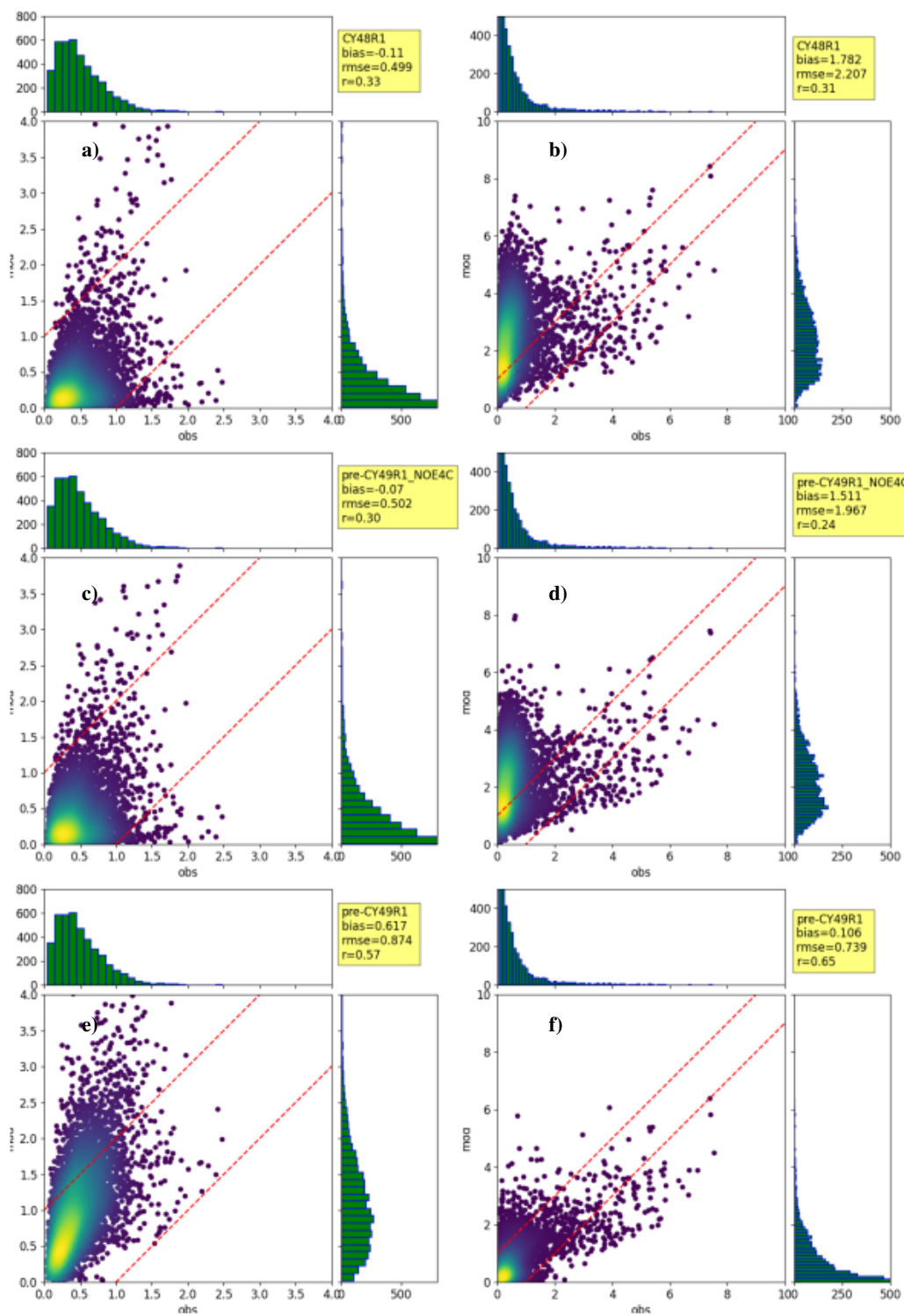
Figure 11. Density scatterplots of the simulated vs observed weekly surface HNO₃ (left) and NO₃⁻ (right) over all 93 CASTNET stations for 2019. Top, CY48R1, middle, CY49R1_NOE4C, bottom, CY49. Units are in $\mu g/m^3$. The dashed red lines demarcate the area where the error is less than 1 $\mu g/m^3$
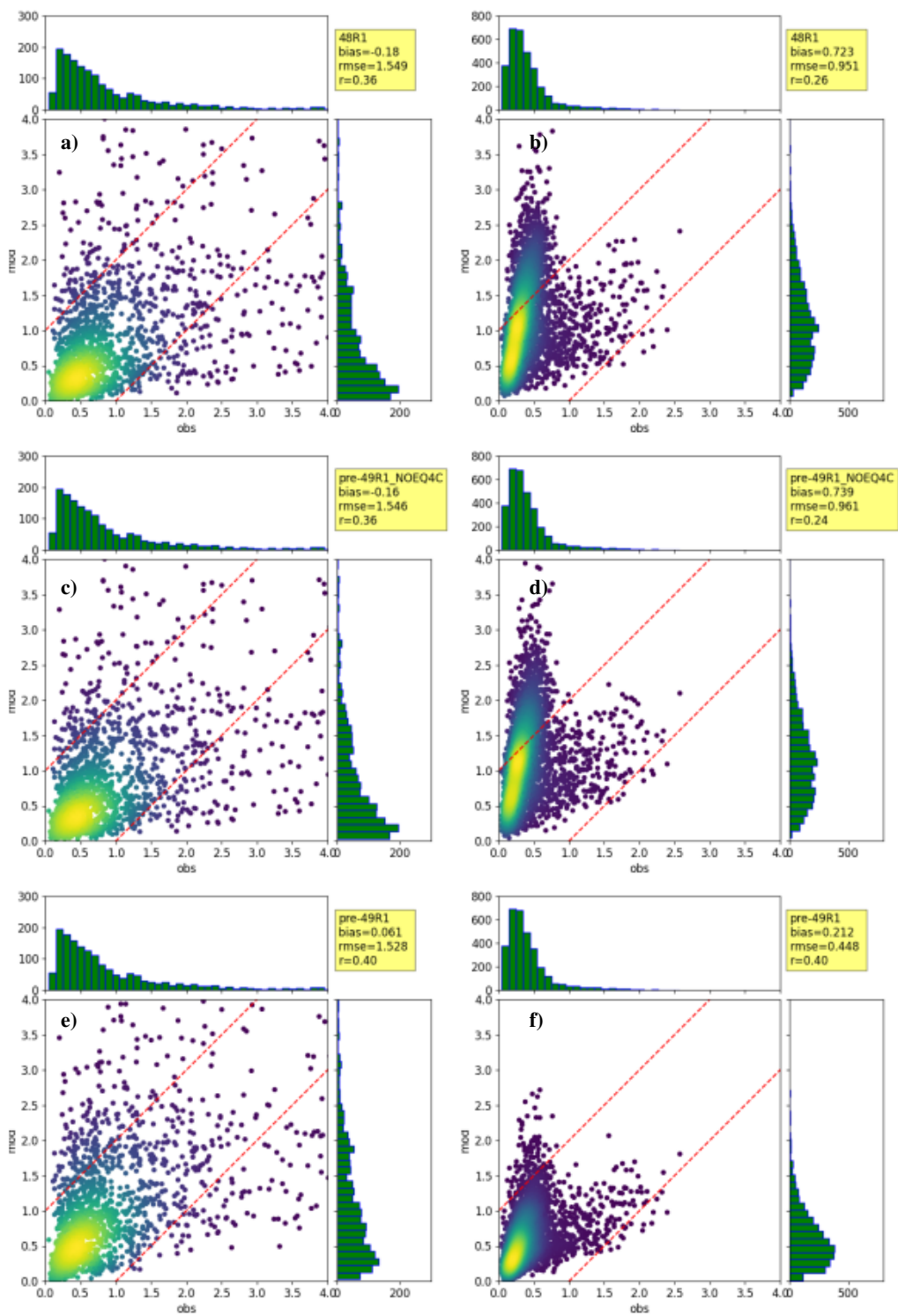
Figure 12. Density scatterplot of simulated vs observed weekly surface NH$_3$ (left) and NH$_4^+$ (right) over all collocated CASTNET and AMoN stations (72 stations in all) for 2019. Top, CY48R1, middle, CY49R1_NOE4C, bottom, CY49. Units are in $\mu g/m^3$. The dashed red lines demarcate the area where the error is less than 1 $\mu g/m^3$.
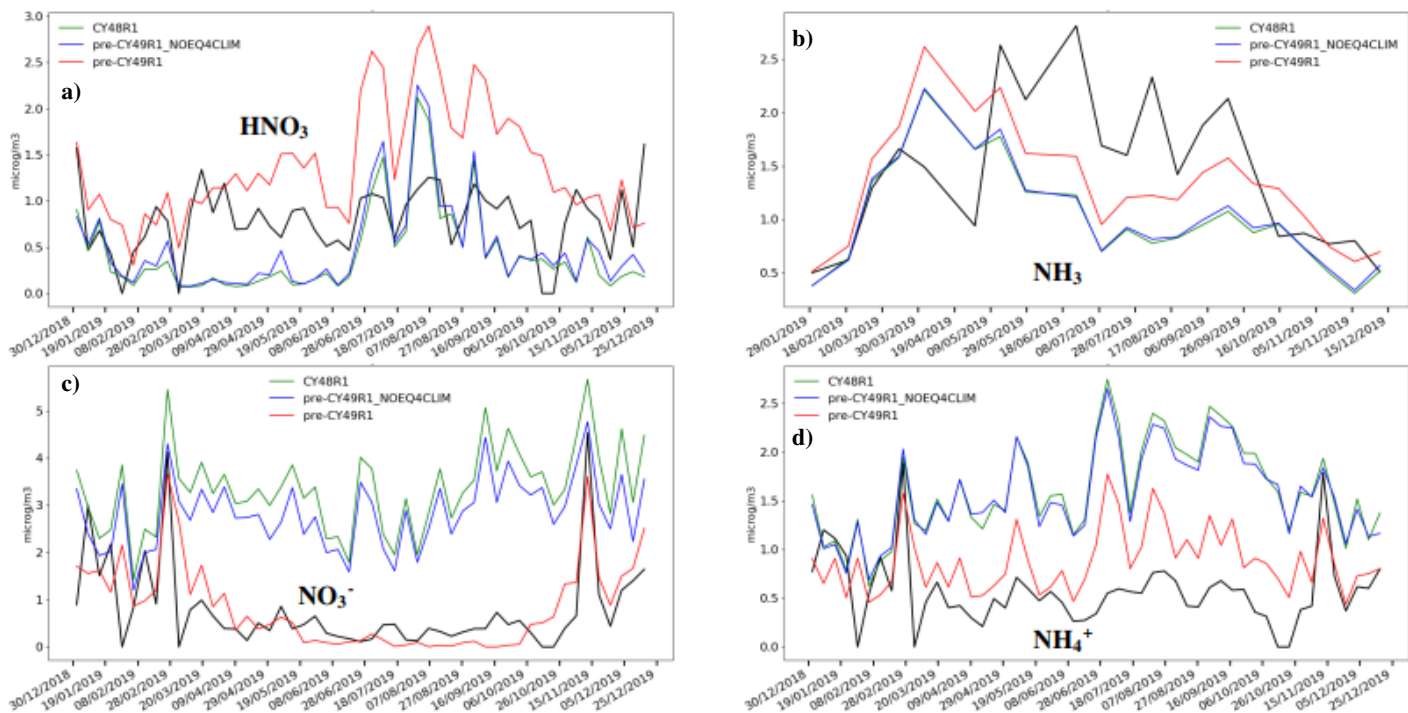
Figure 13. Weekly timeseries of simulated vs observed (solid black line) surface concentration of HNO_3/NO_3^- (left, panels a and c) and NH_3/NH_4^- (right, panels b and d) at the CASTNET/AMoN Mackville site (Kentucky, US). Units are in $\mu g/m^3$.
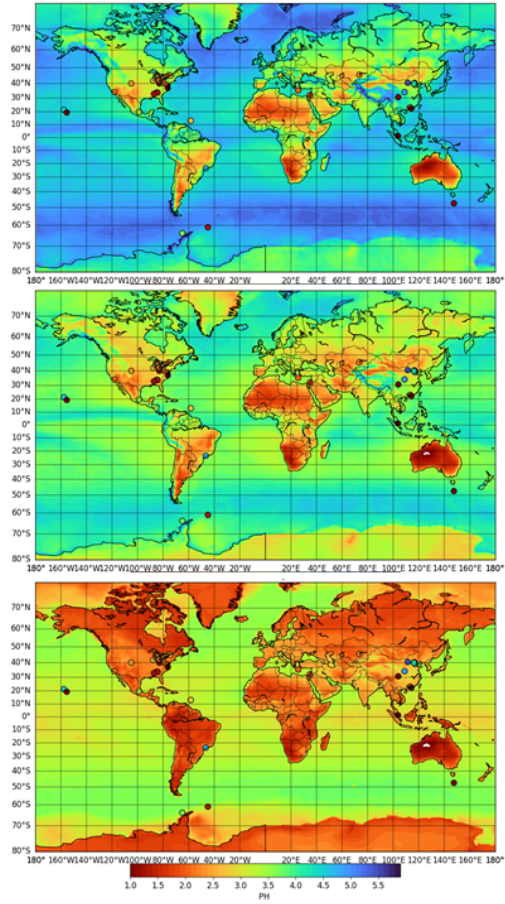
Figure 14. Comparison of simulated global mean 2019 surface aerosol pH from CY49R1 (top), from ISORROPIA-II (middle) and the AERCHEM (bottom) thermodynamical models. The bottom two use data provided by Rosanka et al. (2024) for the year 2010, and only for fine mode aerosols. Climatological surface aerosol pH observations provided by Pye et al. (2020) are also shown in circles.
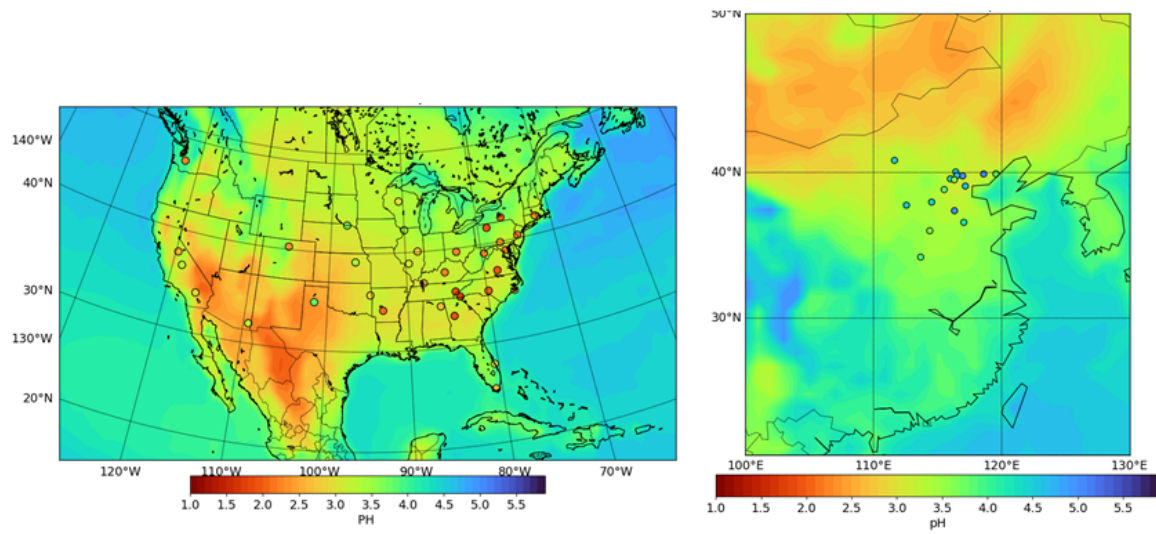
Figure 15. Regional comparisons of surface aerosol pH simulated by CY49R1 averaged in 2019 against 2011 surface data from sites in the U.S. (left) in circles taken from Zhang et al. (2021); right, comparison against 2017 surface data from the Zhang et al. (2021) dataset over China (in circles).
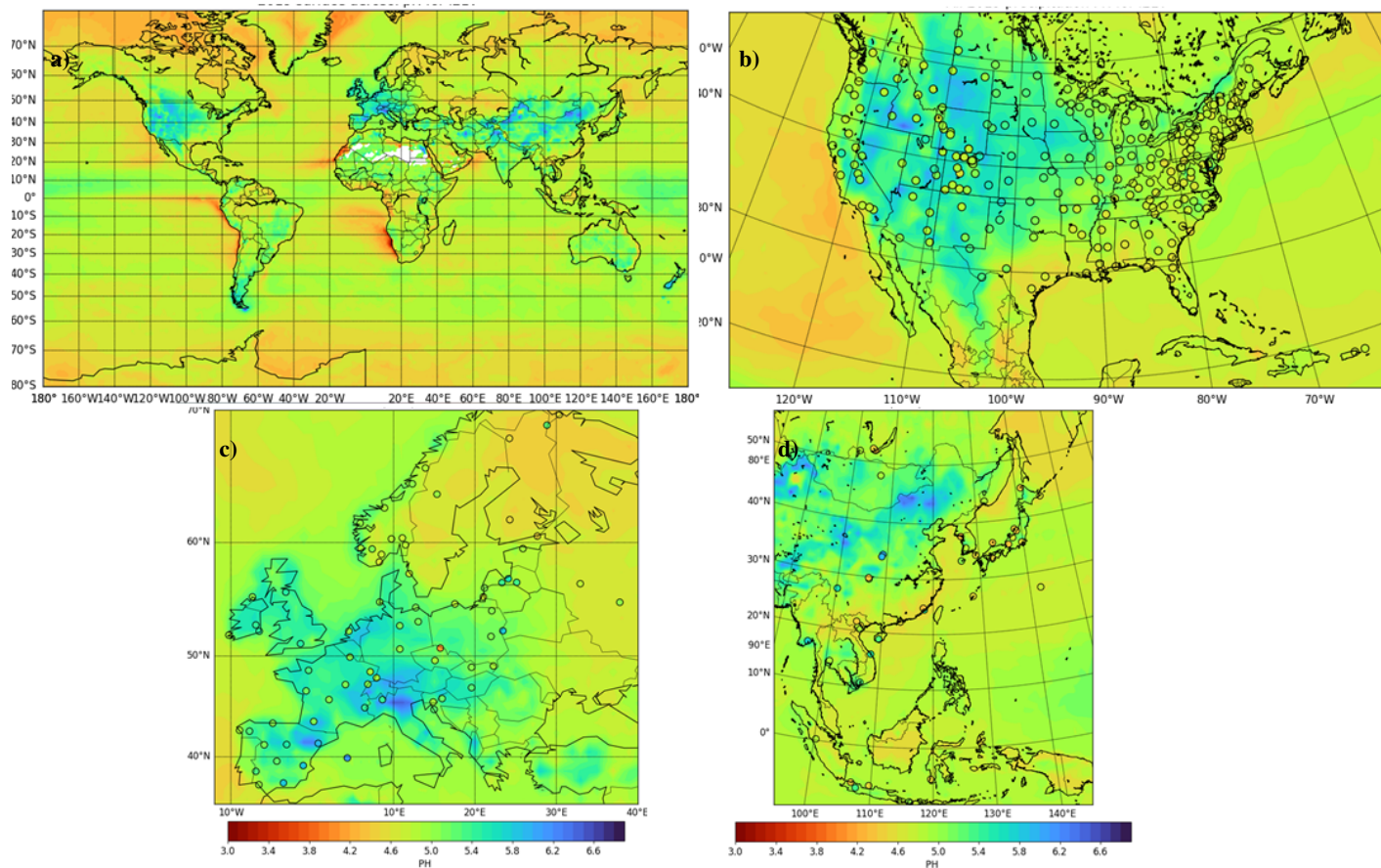
Figure 16. Panel a: global mean surface precipitation pH (top left) simulated in CY49R1 for 2019. Comparisons against the annual mean observational means for US, South-East Asia and Europe are shown in the top right, bottom left and bottom right panels (b,c,d), respectively. The respective observational mean values are shown in the circles, with the details of the regional measurements being described in the text.
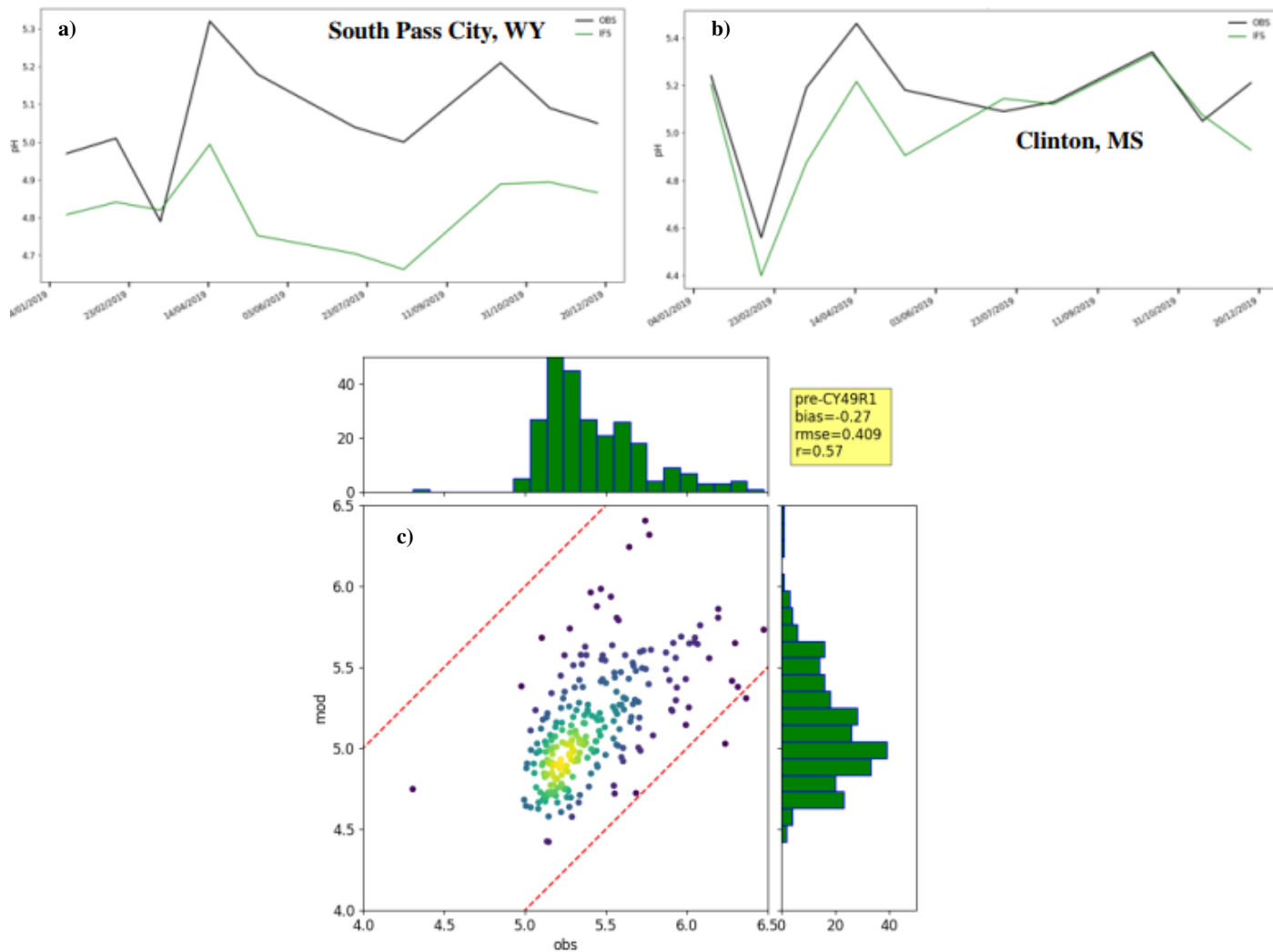
Figure 17. comparison of monthly averaged precipitation pH between simulated and observed values. Panels a and b show monthly comparisons for two NTN/NADP sites in the U.S: South Pass City (Wyoming) and Clinton (Massachusetts). The bottom panel c shows a density scatter plot of simulated vs observed yearly precipitation pH over all 248 NTN/NADP stations in 2019. The dashed red lines demarcate the area where the error is less than 1 pH unit.
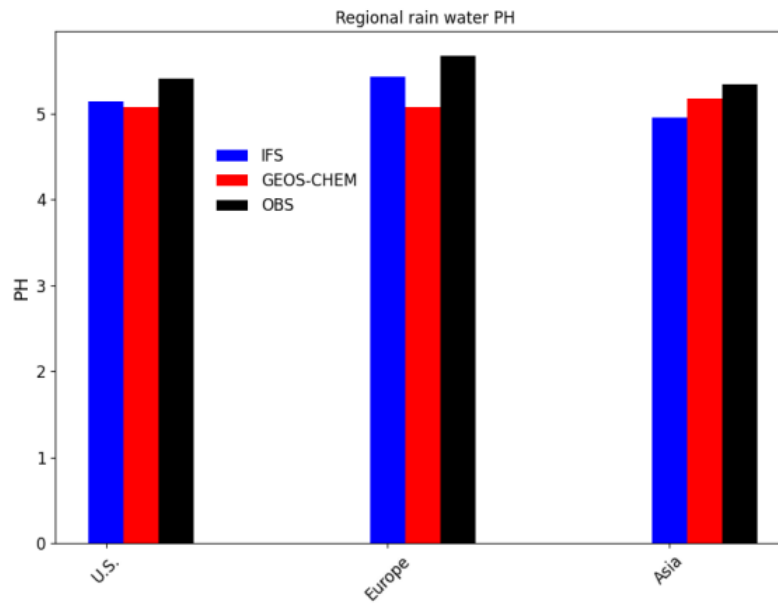
Figure 18. Comparison of regionally averaged precipitation pH as simulated by the CY49R1 experiment and observed by the NADP/NTN (U.S., 248 stations), EANET (East Asia, 49 stations) and EMEP (Europe, 77 stations) networks. GEOS-CHEM simulated precipitation pH for the year 2013, from Shah et al. (2020), is also shown